GEORG-AUGUST-UNIVERSITÄT
GÖTTINGEN

Fakultät für
Physik

Bachelor's Thesis

Untersuchung von systematischen Unsicherheiten in der Suche nach resonanter Higgs Boson Paarproduktion im $b\bar{b}WW^*$ Zerfallskanal

Investigation of systematic uncertainties in the search for resonant di-Higgs production in the $b\bar{b}WW^*$ decay channel

prepared by

Janne van den Hout

from Oldenburg

at the II. Physikalischen Institut

Thesis number:	II.Physik-UniGö-BSc-2021/02
Thesis period:	21st April 2021 until 28th July 2021
First referee:	Prof. Dr. Stan Lai
Second referee:	Prof. Dr. Arnulf Quadt

Abstract

Die Analyse, auf der diese Bachelorarbeit basiert, untersucht mögliche resonante Higgs Boson Paarproduktion mit dem ATLAS Detektor im $HH \to b\bar{b}WW^*$ Zerfallskanal mit einem Lepton im Endzustand in pp-Kollisionen bei $\sqrt{s} = 13\,\text{TeV}$ und einer integrierten Luminosität von $139\,\text{fb}^{-1}$. In dieser Bachelorarbeit wird eine Untersuchung der experimentellen systematischen Unsicherheiten der Analyse präsentiert.

Im ersten Teil der Bachelorarbeit wird die Auswirkung von experimentellen systematischen Unsicherheiten auf eine Auswahl von kinematischen Verteilungen visualisiert und eine Rangliste der systematischen Unsicherheiten mit den größten Auswirkungen erstellt.

Im zweiten Teil der Bachelorarbeit wird eine "non-closure Unsicherheit" für die Schätzung des QCD Untergrundes auf zwei verschiedene Weisen bestimmt. Das erste Vorgehen bestimmt die Unsicherheit der Methode, die zur Schätzung des Hintergrundes verwendet wird. Die zweite Variante beschreibt die Unsicherheit der schlussendlichen Diskriminantenverteilung $m^{HH}_{\text{vis+met}}$, die die Masse des HH Systems ist, berechnet aus den sichtbaren Zerfallsprodukten und der fehlenden transversalen Energie.

Abstract

The analysis this thesis is based on examines possible resonant production of Higgs boson pairs at the ATLAS experiment in the $HH \to b\bar{b}WW^*$ decay channel with a single lepton in the final state in pp-collisions at $\sqrt{s} = 13\,\text{TeV}$ and an integrated luminosity of $139\,\text{fb}^{-1}$. In this thesis an investigation into the experimental systematic uncertainties of the analysis is presented.

In the first part of the thesis the impact of the experimental systematic uncertainties on a selected set of kinematic distributions is visualised and a ranking of the systematic uncertainties with the largest impact is obtained.

In the second part of the thesis, a non-closure uncertainty for the QCD background estimation of the analysis is derived using two different approaches. The first approach determines the uncertainty of the estimation method itself. The second approach determines the uncertainty on the final discriminating distribution $m^{HH}_{\text{vis+met}}$, which is the mass of the HH system calculated from the visible decay products and the missing transverse energy.

Contents

1. Introduction

The Standard Model of particle physics seeks to describe the fundamental particles of the universe and their interactions. Many of the predictions of the Standard Model have been verified by experiments. One example is the discovery of the Higgs boson in 2012 [1, 2], which had already been predicted in the 1960's [3, 4] as a means to give mass to the W and Z boson. There are, however, phenomena that the Standard Model is not able to explain. Consequently, new theories are investigated which consider additional Higgs bosons. The Standard Model as well as these extended theories predict the production of Higgs boson pairs.

The analysis on which this thesis is based, searches for resonant Higgs pair production with the ATLAS detector in the $HH \to b\bar{b}WW^*$ decay channel, where an unknown heavy particle decays into two Higgs bosons. The result of every ATLAS analysis is subject to statistical and systematic uncertainties. While statistical uncertainties are related to the number of events detected, systematic uncertainties arise from imperfect modelling or calibration of the measurement instruments as well as incomplete theoretical knowledge. The estimation of the systematic uncertainties is therefore a relevant part of every analysis.

In this thesis, an investigation into the experimental systematic uncertainties of the analysis is presented. The thesis is divided into two parts. The first part is concerned with the impact of the systematic uncertainties on certain kinematic distributions and the quantification of this impact. In the second part of the thesis a non-closure uncertainty for the QCD background estimate is obtained using two different approaches.

In Chapter 2, an overview of the Standard Model and the Higgs mechanism is given. Furthermore, theories extending the Standard Model and the processes for Higgs boson pair production are presented. In Chapter 3, the LHC as well as the most important components of the ATLAS detector are described. The decay channel, object definitions, event selection and the background estimation of the analysis are outlined in Chapter 4. The impact of the systematic uncertainties on certain kinematic distributions of the analysis is discussed in Chapter 5. Chapter 6 presents the derivation of the non-closure uncertainty for the QCD background estimate using two different approaches. Finally, a brief summary of the results is given in Chapter 7.

2. The Standard Model of Particle Physics

The Standard Model (SM) combines elementary particles and their interactions in a single model. It describes the electromagnetic, weak nuclear and strong nuclear interactions; the fourth fundamental force gravity is not a part of the SM. Although the SM is not a complete theory, many of its predictions have been verified by experiments.

In Section 2.1 of this chapter, a brief overview of the elementary particles of the SM and their fundamental interactions is given. Sections 2.2 and 2.3 contain a description of the Higgs mechanism and Higgs boson. Finally, limitations of the SM and possible extensions are discussed as well as the possibility of Higgs boson pair production.

2.1. Elementary particles and their fundamental interactions

According to the SM, there are twelve spin-½ fermions as well as bosons with integer spin. The fermions can be divided into two groups: leptons and quarks. For each fermion there is a corresponding antifermion with the same mass but opposite electric charge. Charged leptons such as electrons, muons, and tauons carry an electric charge of -1. They each have an associated electrically neutral neutrino. Besides carrying an electric charge of $\frac{2}{3}$ or $-\frac{1}{3}$ quarks also carry a colour charge. Unlike leptons, quarks are never found alone but combine together to form hadrons. Furthermore, the fermions can be assigned to three generations. The first generation is made up of the up and down quark, the electron neutrino and the electron. The charm and strange quark, the muon neutrino and the muon belong to the second generation. The third generation consists of the heavy top and bottom quark, the tau neutrino and the tauon. The particles in a higher generation each have a larger mass than the corresponding particle in a lower generation.

The bosons of the SM are made up of one spin-0 scalar boson and multiple spin-1 gauge bosons. The gauge bosons are the mediators of the fundamental forces. The photon mediates the electromagnetic interaction between charged particles. Gluons couple

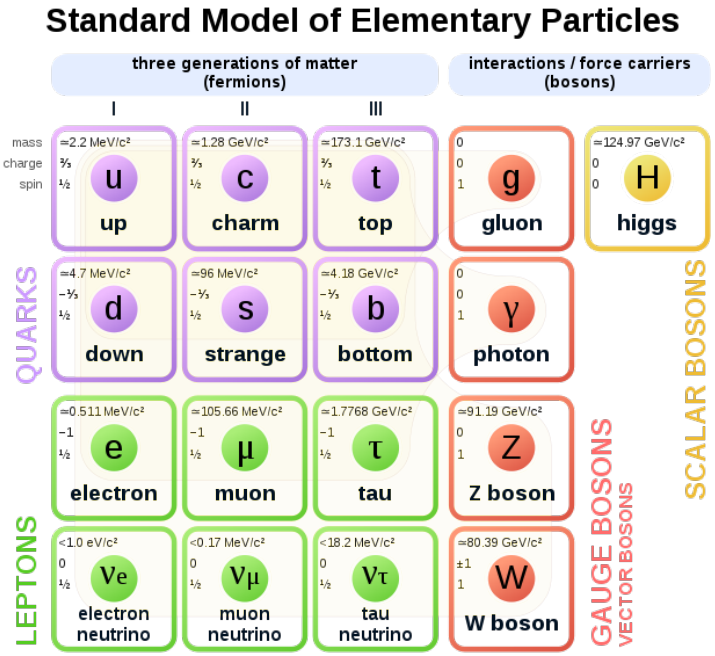

Figure 2.1.: Depiction of the elementary particles of the SM. For every particle the mass, charge and spin are given. Fermions in one column belong to the same generation [5].

together particles with a colour charge giving rise to the strong force, while the $W^{\pm}$ and Z bosons mediate the weak interaction [6]. The spin-0 scalar boson is the Higgs boson which plays an important role in the SM and will be discussed later on in this chapter. An overview of the elementary particles, their masses, charge, and spin is given in Figure 2.1.

In the SM, the electromagnetic, weak and strong nuclear interaction each corresponds to a local gauge symmetry of the underlying quantum field theory. The requirement that the Lagrangian of the theory is invariant under a local phase transformation gives rise to gauge fields. The excitations of these fields are the gauge bosons that mediate the interaction.

The field theory describing the electromagnetic interaction is quantum electrodynamics (QED), which is required to be invariant under local U(1) transformations. To ensure this invariance, a gauge field is introduced that corresponds to the covariant four-potential A_μ of the electromagnetic field. The excitations of this gauge field are the neutral and massless photons that mediate the electromagnetic interaction between charged fermions.

The strong interaction is described by quantum chromodynamics (QCD). It is the strongest interaction in the SM and only couples to particles carrying a colour charge.

There are three different colour charges red (r), blue (b) and green (g), and antiparticles carry a corresponding anti-colour charge. In QCD, the Lagrangian is invariant under local SU(3) phase transformations. For each of the eight generators of the SU(3) symmetry group arises a corresponding gauge field - the gluon fields. The quantisation of these fields leads to eight massless gluons carrying colour charge [7]. Particles carrying colour charge cannot be observed on their own, but clump together instead to form colour neutral hadrons which become visible as jets in particle detectors. This phenomenon is known as colour confinement. It can be explained by the fact that the energy stored in the gluon field between colour charged particles increases with the distance between them. At large energies quark-antiquark pairs are created and the gluon field breaks into smaller "strings" [8].

The weak interaction is mediated by the charged $W^{\pm}$ and neutral Z bosons. The weak force couples together fermions differing in weak isospin, making it the only interaction capable of changing the flavour of quarks. In contrast to the photon and gluons, which are massless as required by the local gauge invariance, the $W^{\pm}$ and Z boson have a mass of 80.4 GeV and 91.2 GeV [9], respectively. They obtain their mass through interaction with the Higgs boson (see Section 2.2). The $W^{\pm}$ bosons only couple to left-handed chiral particles or right-handed chiral antiparticles. The symmetry group of the charged-current weak interaction theory is referred to as $\mathrm{SU}(2)_L$ which is generated by the weak isospin. The invariance under this symmetry leads to three gauge fields W^1_μ, W^2_μ and W^3_μ from which the charged $W^{\pm}$ fields can be constructed

$$W^{\pm}_\mu = \frac{1}{\sqrt{2}}(W^1_\mu \mp W^2_\mu) \ .$$

The remaining neutral field W^3_μ cannot be identified with the field corresponding to the Z boson, as experiments have shown that the Z boson couples to both left- and right-handed particles. However, by combining the theory for electromagnetism and the weak interaction the Z-boson field can be constructed.

In a unified description of the electromagnetic and weak interaction [10–12] called the electroweak interaction, the U(1) gauge symmetry of the electromagnetic interaction is replaced by $\mathrm{U}(1)_Y$. Instead of coupling to the electric charge Q, the gauge field B_μ couples to the weak hypercharge $Y = 2(Q - T_3)$, where T_3 is the third component of the weak isospin. The underlying symmetries of the electromagnetic and weak interaction are combined into a $\mathrm{SU}(2)_L \times \mathrm{U}(1)_Y$ group. The photon field A_μ and Z-boson field Z_μ can

then be written as linear combinations

$$\begin{aligned} A_\mu = &\quad B_\mu \cos(\theta_\mathrm{W}) + W^3_\mu \sin(\theta_\mathrm{W}) \\ Z_\mu = &-B_\mu \cos(\theta_\mathrm{W}) + W^3_\mu \cos(\theta_\mathrm{W}) \end{aligned}$$

of the neutral fields B_μ and W^3_μ, and the weak mixing angle θ_W.

The SM describes both the electroweak and strong interactions, and is therefore a quantum field gauge theory with the symmetry group $\mathrm{U}(1)_Y \times \mathrm{SU}(2)_L \times \mathrm{SU}(3)$.

2.2. Higgs mechanism

The explanations in this section are based on the derivation used in Ref. [8]. As discussed in the previous section, the invariance under $\mathrm{SU}(2)_L \times \mathrm{U}(1)_Y$ symmetry transformations in the electroweak theory gives rise to four massless gauge fields. However, the observed $W^\pm_\mu$ and Z bosons are amongst the heaviest particles in the SM. To generate the masses of these gauge bosons the Higgs mechanism is embedded in the theory. For this, a doublet of complex scalar fields

$$\phi(\boldsymbol{x}) = \frac{1}{\sqrt{2}} \begin{pmatrix} \phi_1(\boldsymbol{x}) + i\phi_2(\boldsymbol{x}) \\ \phi_3(\boldsymbol{x}) + i\phi_4(\boldsymbol{x}) \end{pmatrix}$$

is added to the Lagrangian. The four degrees of freedom are required to ultimately obtain a massive scalar field and three massless Goldstone bosons, which give the $W^\pm_\mu$ and Z bosons their longitudinal degree of freedom. Furthermore a potential

$$V(\phi) = \mu^2 \phi^\dagger \phi + \lambda (\phi^\dagger \phi)^2$$

of the field is added with $\mu^2 < 0$ and $\lambda > 0$. It can be shown that the minimum for this potential does not occur at $\phi(\boldsymbol{x}) = 0$ but at a distance $v = \sqrt{\frac{-\mu^2}{\lambda}}$ from the origin. The field $\phi(\boldsymbol{x})$ is said to have a non-zero vacuum expectation value.

If the quantum fields of the theory are expressed as an expansion around a vacuum state, the $\mathrm{SU}(2)_L \times \mathrm{U}(1)_Y$ symmetry of the Lagrangian is not apparent anymore, but rather hidden. This process is called spontaneous symmetry breaking. The resulting Lagrangian contains three massive gauge boson fields, as well as the aforementioned massive scalar field and three Goldstone bosons. The Lagrangian can be simplified by writing the expansion around the vacuum state in unitary gauge

$$\phi(\boldsymbol{x}) = \frac{1}{\sqrt{2}} \begin{pmatrix} 0 \\ v + h(x) \end{pmatrix}$$

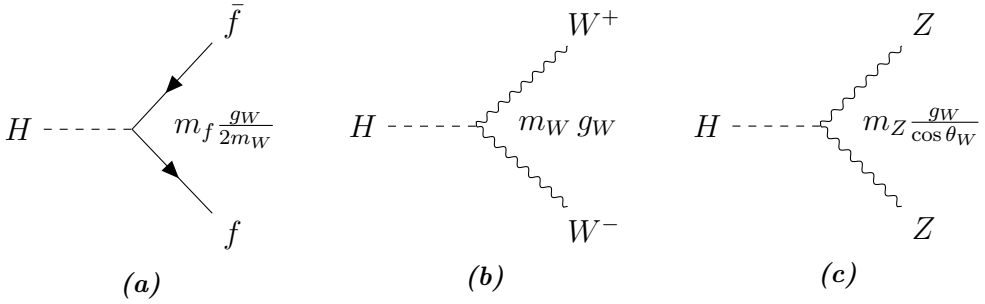

Figure 2.2.: Lowest-order Feynman diagrams for Higgs boson interaction with fermions (a), $W^{\pm}$ bosons (b) and Z bosons (c).

where $h(x)$ is the Higgs field. The resulting Lagrangian only consists of terms corresponding to physical particles. From the terms of the electroweak gauge fields, the masses

$$m_W = \frac{1}{2} g_W v$$
$$m_Z = \frac{1}{2} \frac{g_W}{\cos\theta_W} v$$

of the $W^{\pm}_{\mu}$ and Z bosons can be determined at leading order, with g_W being the weak coupling constant. The photon remains massless as required. The mass of the Higgs boson at leading order

$$m_H = \sqrt{2\lambda} v$$

can also be inferred. Furthermore, the Lagrangian contains self-interaction terms for the Higgs boson and interaction terms between the Higgs and gauge bosons from which the coupling strengths can be determined. The interaction vertices and corresponding coupling strengths are shown in Figure 2.2.

Similarly, the Higgs mechanism can be used to generate the masses of the SM fermions. The coupling of the fermion to the Higgs field generates the fermion mass

$$m_f = \frac{1}{\sqrt{2}} g_f v \ ,$$

where g_f is the Yukawa coupling constant.

2.3. Higgs boson production and decay

In 2012, the Atlas and Cms experiments at the Lhc both reported the discovery of a new particle that exhibited the Higgs boson properties predicted by the SM [1, 2]. Using

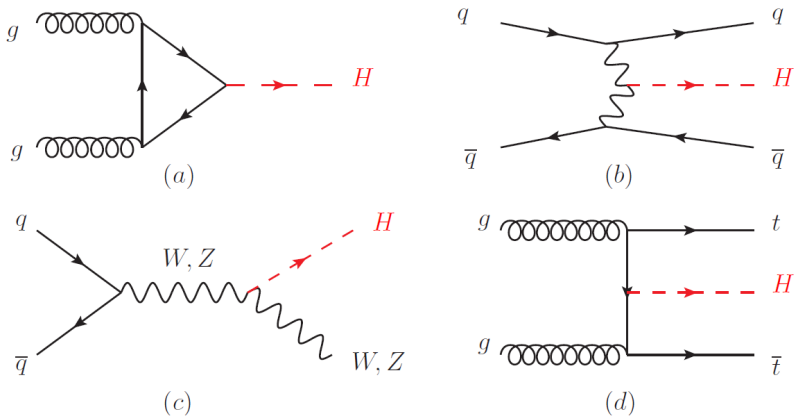

Figure 2.3.: Lowest-order Feynman diagrams for the Higgs production modes ggF (a), VBF (b), VH (c) and $t\bar{t}H$ (d) at the LHC at $\sqrt{s} = 13\,\text{TeV}$ [9].

the combined data samples gathered by the experiments during Run 1, the mass of the Higgs boson was estimated to be $m_H = 125.09 \pm 0.21\,(\text{stat.}) \pm 0.11\,(\text{syst.})\,\text{GeV}$ [13].

The SM predicts different mechanisms by which a Higgs boson can be produced. The lowest-order Feynman diagrams for the dominant production processes are shown in Figure 2.3. The production mode with the largest cross section and therefore the most common process at the LHC is gluon-gluon fusion (ggF). Two gluons can give rise to a virtual top quark loop which then yields a Higgs boson in the final state. The process with the second highest cross section at the LHC is vector-boson fusion (VBF). Two quarks from the collision each radiate a vector boson either a $W^{\pm}$ boson or a Z boson, which then couple to the Higgs boson. Additionally, vector-boson associated production (VH) which is the radiation of a Higgs boson from a $W^{\pm}$ or Z boson and associated top pair production ($t\bar{t}H$) are observed at the LHC.

The predicted cross sections for the different Higgs boson production modes in pp collisions for a centre-of-mass energy of $\sqrt{s} = 13\,\text{TeV}$ and $m_H = 125\,\text{GeV}$ are given in Table 2.1. The total Higgs boson production cross section is 50.6 pb [14].

Once produced, the Higgs boson decays quickly due to its relatively large mass. As can be seen in Figure 2.2, the Higgs boson can decay into a fermion-antifermion pair as well as into two oppositely charged W bosons or two Z bosons. It can also be seen that the coupling strength depends on the fermion's, W or Z boson's mass. The decay into a W boson pair is suppressed because one of the decay products will be a virtual (off-shell) particle W^* since $m_H < 2m_W$. The same holds for the decay into ZZ^*. The decay with the highest branching ratio is therefore the fermionic decay into a $b\bar{b}$ pair.

Table 2.1.: Cross sections for the different Higgs boson production processes in pp collisions for $\sqrt{s} = 13\,\text{TeV}$ and $m_H = 125\,\text{GeV}$. The total Higgs boson production cross section is 50.6 pb [14].

Production mode	Cross section [pb]
ggF	44.1
VBF	3.78
WH	1.37
ZH	0.88
$t\bar{t}H$	0.51

The Higgs boson can also decay into massless particles such as gluons and photons via virtual top quark and W boson loops. The branching ratios for the main decay modes of a Higgs boson with mass $m_H = 125\,\text{GeV}$ are given in Table 2.2.

Table 2.2.: Decay modes of the Higgs boson and their corresponding branching ratios for $m_H = 125\,\text{GeV}$ [14].

Decay mode	Branching ratio
$H \to b\bar{b}$	58.4 %
$H \to WW^*$	21.4 %
$H \to gg$	8.6 %
$H \to \tau^+\tau^-$	6.2 %
$H \to c\bar{c}$	2.9 %
$H \to ZZ^*$	2.6 %
$H \to \gamma\gamma$	0.2 %

2.4. Beyond the Standard Model

Many predictions of the SM have been confirmed by experiments, however, the SM is not a complete theory. Of the four fundamental forces, only three are described by the SM. Gravity is not part of the SM, because so far accommodating the theory of general relativity into the SM has proven to be difficult. The SM is also not a fully unified theory since it is based on the $\text{U}(1)_Y \times \text{SU}(2)_L \times \text{SU}(3)$ symmetry group. For a fully unified theory, however, one would expect a single underlying gauge symmetry to describe all three interactions [15].

Furthermore, there is experimental evidence that a significant fraction of the mass in the universe is non-baryonic and non-luminous. This is known as dark matter and is

assumed to consist of weakly interacting massive particles (WIMPs) [16], with properties inconsistent with any of the SM particles.

To solve these problems, theories extending the SM are considered. Supersymmetry (SUSY) is such a possible extension. In supersymmetric models every particle of the SM has a super-partner whose spin differs by $\frac{1}{2}$. Models including supersymmetry, such as the Minimal Supersymmetric Standard Model (MSSM), can solve the hierarchy problem [17]. Furthermore, if R-parity is conserved, the MSSM provides a candidate particle for dark matter. In supersymmetric models a second Higgs doublet has to be added to give mass to both up- and down-type quarks and cancel anomalies [18]. In addition, the second doublet is able to generate the baryon asymmetry which cannot be explained by the SM [19].

Two-Higgs-doublet models (2HDM) are simple extensions of the SM, which can also include supersymmetry. In 2HDMs, a second doublet of complex scalar fields is added to the SM. As described in Section 2.2, the doublet fields can be expanded around the two vacuum expectation values leading to spontaneous symmetry breaking. The eight degrees of freedom of the two doublets result in three Goldstone bosons giving mass to the $W^{\pm}$ and Z bosons like before. The remaining five degrees of freedom result in physical scalar fields corresponding to five Higgs bosons: two neutral CP-even scalars h and H^0, two charged scalars $H^{\pm}$, and a neutral CP-odd pseudoscalar A^0 [18].

2.5. Higgs boson pair production

Until now, only single Higgs boson production has been observed. However, the SM predicts Higgs boson self-interactions (see Section 2.2) and therefore the possibility of non-resonant Higgs boson pair production. The dominant production mode for Higgs pair production in proton-proton collisions at the LHC is gluon-gluon fusion. The two lowest-order Feynman diagrams for Higgs boson pair production are shown in Figure 2.4.

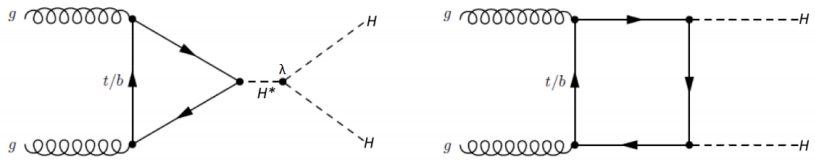

Figure 2.4.: Lowest-order Feynman diagrams for non-resonant Higgs boson pair production via gluon-gluon fusion [20].

One possible process is the coupling of two gluons to an off-shell Higgs boson via

a heavy quark loop. Due to the self-interaction, the virtual Higgs boson decays into two massive Higgs bosons. The study of this decay makes it possible to measure the self-coupling parameter λ, which determines the shape of the Higgs potential. Another possible process is Higgs boson pair production via a top quark loop with two $t\bar{t}H$ vertices. As the two Higgs bosons do not couple, this process does not allow for the study of the self-coupling parameter. The amplitudes for both Higgs boson pair production processes interfere destructively resulting in a small predicted cross section for ggF of 31.05 fb in pp collisions at 13 TeV [21].

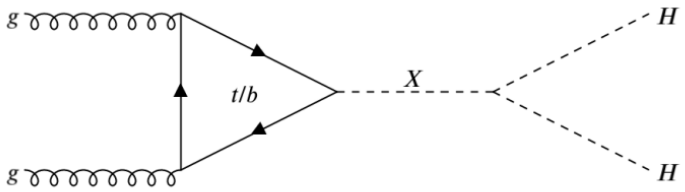

Figure 2.5.: Lowest-order Feynman diagrams for resonant Higgs boson pair production via gluon-gluon fusion.

In theories beyond the SM, Higgs boson pair production is also possible through resonant production where a heavy particle produced during the collision decays into two Higgs bosons. For example in the MSSM a H^0 boson could decay into two lighter h bosons [22]. Figure 2.5 shows the lowest order Feynman diagram for resonant Higgs boson pair production via gluon-gluon fusion, where an unknown particle X decays into two Higgs bosons.

3. Experimental Setup

The ATLAS experiment is one of the four major experiments at the Large Hadron Collider (LHC) at CERN. In the following, a short overview of the LHC and the most important components of the ATLAS detector is given.

3.1. The Large Hadron Collider

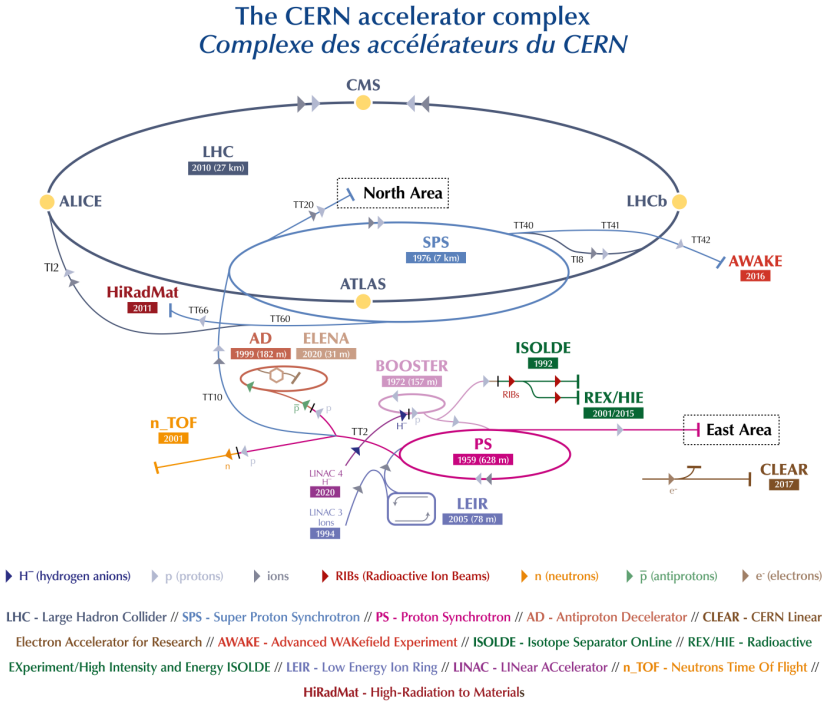

Figure 3.1.: Sketch of the accelerator chain at CERN and the experiments at the LHC [23].

The Large Hadron Collider (LHC) [24] is the world's largest particle accelerator. The LHC was designed with a luminosity of $10^{34}\,\mathrm{cm}^{-2}\mathrm{s}^{-1}$ and a centre-of-mass energy of 14 TeV to produce heavy particles such as the Higgs boson and reveal physics beyond the SM among other things.

It was built by the European Organisation for Nuclear Research (CERN) between 1998 and 2008. The LHC is a circular proton-proton collider with a circumference of 27 km. It is situated in a tunnel approximately 100 m below the ground to shield it from radiation. The LHC consists of two beam pipes being kept at an ultra high vacuum in which two proton beams travel in opposite directions. Acceleration structures along the ring increase the energy of the protons, while magnetic fields of 8.33 T produced by superconducting magnets keep the particles on their circular path. Liquid helium is used to cool the magnets down to their operating temperature of 1.9 K.

Before being injected into the LHC, the proton beams pass through a chain of accelerators (see Figure 3.1). Each accelerator increases the energy of the beam before injecting it into the next one. The first accelerator in the chain is LINAC 2 [1] which accelerates the beams to an energy of 50 MeV. After this, the proton beams are injected into the Proton Synchroton Booster which increases their energy to 1.4 GeV. The beam is then fed to the Proton Synchrotron which accelerates it to 25 GeV. Subsequently, the beam passes through the Super Proton Synchrotron which increases the energy to 450 GeV. Lastly, the proton beams are injected into the LHC and accelerated to their final energy of 6.5 TeV.

Along the ring, there are four points at which the two beam pipes intersect and the two proton beams are made to collide. During Run 2 of the LHC, the two proton beams collided at a centre-of-mass energy of $\sqrt{s} = 13$ TeV. Around the collision points detectors are installed belonging to one of the four major experiments. ATLAS and CMS are multi-purpose experiments while the ALICE experiment studies quark-gluon plasma and LHCb investigates b-physics.

3.2. The ATLAS detector

The ATLAS detector [25] is a general-purpose particle detector at the LHC designed to record the trajectory, momentum, and energy of the particles produced in the collisions. The most important components of the detector are: the inner detector (ID), which is made up of the pixel detector, the semiconductor tracker and the transition radiation tracker, the electromagnetic and hadronic calorimeters, and the muon spectrometer. A depiction of the ATLAS detector and the main components can be seen in Figure 3.2. In the centre region, also called the barrel region, the detectors are arranged in concentric cylinders around the beam pipe. At each side are the end caps, with sensors that are located on discs perpendicular to the beam axis.

[1] LINAC 2 is replaced by LINAC 4 for the next run starting in 2022. LINAC4 will accelerate the beams to an energy of 160 MeV.

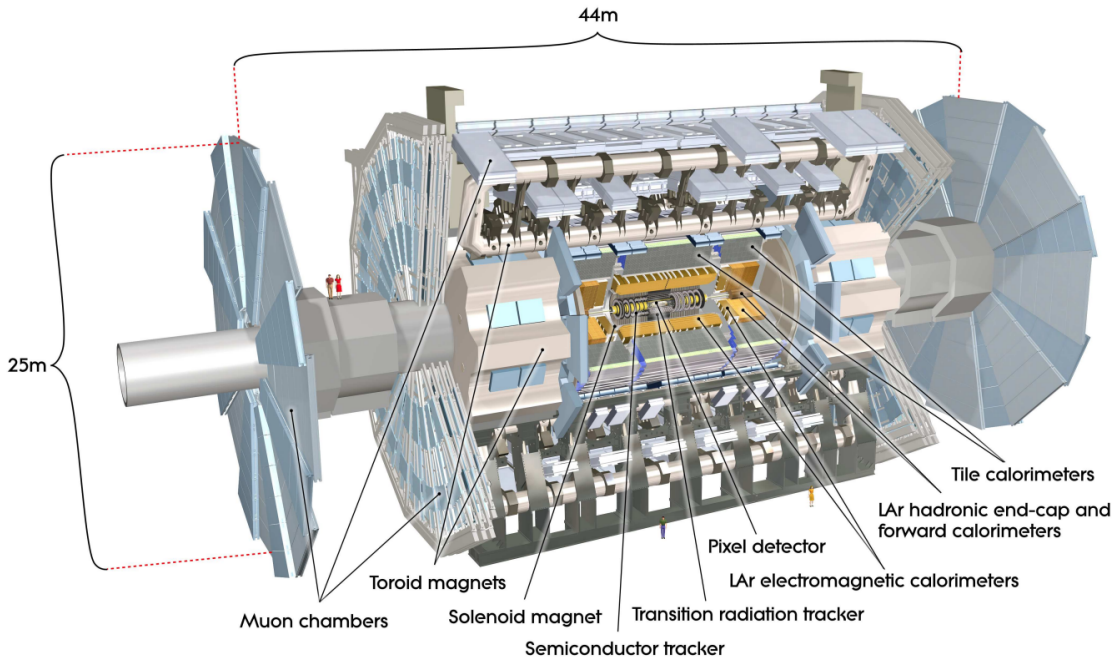

Figure 3.2.: General layout of the ATLAS detector and its components [25].

Coordinate system and physical quantities

The ATLAS detector uses a special coordinate system. The collision point is defined as the origin of the coordinate system. The transverse plane is defined by the x-axis which points from the origin towards the centre of the LHC and the y-axis which points upwards. Using a right-handed coordinate system the $+z$-axis is therefore well-defined and parallel to the particle beams. Other parameters used are θ, the polar angle with respect to the z-axis and ϕ, the azimuthal angle in the transverse plane.

Relevant physical quantities are the rapidity $y = \frac{1}{2} \ln \left(\frac{E+p_z}{E-p_z} \right)$ of a particle with energy E and momentum p_z in the beam direction. The difference in rapidity Δy is Lorentz invariant under boosts in the longitudinal direction. The pseudorapidity is defined as $\eta = -\ln \left[\tan \left(\frac{\theta}{2} \right) \right]$. In the relativistic limit $\eta \approx y$ holds and therefore the difference $\Delta\eta$ is approximately invariant under Lorentz boosts in the longitudinal direction. For this reason the pseudorapidity is preferred over the polar angle θ. Given $\Delta\eta$, the distance $\Delta R = \sqrt{(\Delta\eta)^2 + (\Delta\phi)^2}$ between two particles in the $\eta - \phi$ plane can be defined. The transverse momentum p_T is the component of the momentum transverse to the beam direction and the transverse energy is defined as $E_T = E \sin(\theta)$.

Inner detector

The inner detector system is located closest to the beam pipe. It extends from an inner radius of 5 cm to an outer radius of 1.2 m and has a length of 6.2 m. The ID is immersed in a 2 T magnetic field produced by a superconducting solenoid magnet system. Due to the magnetic field, the trajectories of charged particles are curved. The charge of the particle can be inferred from the direction of the curvature. By measuring the tracks of the particles with the inner detector, the transverse momentum p_T can be inferred from the curvature. Furthermore, the inner detector provides vertex measurements, which are used to determine the point of collision (primary vertex) and vertices originating from the decay of e.g. b hadrons (secondary vertices). The inner detector consists of three individual sub-detectors: the pixel detector, the semiconductor tracker (SCT), and the transition radiation tracker (TRT). The detector located closest to the collision point is the silicon pixel detector. It consists of four layers in the barrel region and three discs in each of the two end cap regions. The silicon pixels in the innermost layer have a size of $50 \times 250\,\mu\text{m}^2$ while the pixels in the three external layers have a size of $50 \times 400\,\mu\text{m}^2$. There are 2024 pixel modules in the pixel detector each containing approximately 46000 pixels. With 92 million readout channels for these pixels, the pixel detector provides precise tracking. The pixel detector is surrounded by the SCT which uses narrow silicon strips with a pitch of $80\,\mu$m instead of pixels. Each module in the SCT consists of two layers of strips. One layer of strips is parallel to the beam axis whereas the other layer is rotated at an angle of 40 mrad. The pixel detector and the SCT cover a pseudorapidity range of $|\eta| < 2.5$. The outermost part of the inner detector is the TRT. It is composed of layers of drift tubes filled with ionising gas. The tubes are interleaved with materials with different refraction indices. The produced transition radiation can be used for electron identification. The TRT detects particles with $|\eta| < 2.0$. The relative resolution of the transverse momentum of the inner detector is $\frac{\sigma_{pT}}{p_T} = 0.05\,\%\,p_T \oplus 1\%\,[\text{GeV}]$.

Calorimeters

The calorimeters in the ATLAS detector are positioned outside of the solenoid magnet and measure the energy deposition of the incident particles. The calorimetry system consists of an electromagnetic calorimeter and a hadronic calorimeter each made up of a barrel and end cap region. In addition, there is a forward calorimeter to cover the region closest to the beam. The calorimeters used at ATLAS are sampling calorimeters, which consist of alternating layers of an absorber material responsible for developing the particle showers and an active material measuring the deposited energy.

In the electromagnetic calorimeter, the energy of electrons and photons are measured. Liquid argon is used as active detector material and lead plates are used as absorbers. The absorbers are arranged in an accordion shape to ensure a uniform response of the calorimeters. The barrel region of the electromagnetic calorimeter covers a pseudorapidity range of $|\eta| < 1.475$ while the two end caps cover $1.375 < |\eta| < 3.2$. It provides a relative energy resolution of $\frac{\sigma_E}{E} = \frac{10\,\%}{\sqrt{E}} \oplus 0.7\%\,[\mathrm{GeV}]$.

The hadronic calorimeters detect particles that shower hadronically. In the barrel region scintillating plastic tiles and steel absorbers are used and provide a pseudorapidity coverage for $|\eta| < 1.7$. The hadronic end cap calorimeter consists of liquid argon and copper absorbers and is used for the region $1.5 < |\eta| < 3.2$. In total the hadronic calorimeter provides a relative energy resolution of $\frac{\sigma_E}{E} = \frac{50\,\%}{\sqrt{E}} \oplus 3\%\,[\mathrm{GeV}]$.

The pseudorapidity range $3.1 < |\eta| < 4.9$ close to the beam is covered by the forward calorimeter which provides both electromagnetic and hadronic energy measurements. It uses liquid argon as active material as well as copper and tungsten as absorbers.

Muon spectrometer

Muons are charged leptons like electrons but approximately 200 times heavier. Therefore, they only lose small amounts of energy due to bremsstrahlung and scattering and pass through the inner detector and calorimeters. For that reason, the chambers to detect muons are the farthest away from the collision point. The muon spectrometer at the ATLAS detector surrounds the calorimeters making it the largest part of the detector with an inner radius of 4.25 m and an outer radius of 11 m. Three air-core toroidal magnets in the muon spectrometer provide a magnetic field of 0.5 T and 1 T for the barrel and end cap region, respectively. The muon spectrometer is made from chambers filled with gas, which is ionised by the traversing muons and thus provides information on the position of the particle. The measurements of the track coordinates are provided by monitored drift tubes in the barrel region for $|\eta| < 1.0$ and partly in the end caps for $|\eta| < 2.0$. At large pseudorapidities of $2.0 < |\eta| < 2.7$, cathode strip chambers with a higher granularity are used.

Besides the chambers for precise measurements, the muon spectrometer also includes a system of trigger chambers for $|\eta| < 2.4$. The resistive plate chambers in the barrel region and the thin gap chambers in the end cap region provide information about the tracks of the muons traversing the detector within 1.5 to 4 ns.

The relative transverse momentum resolution achieved by the muon spectrometer is approximately 10 % for muons with $p_T = 1\,\mathrm{TeV}$.

Trigger system

The proton-proton collision rate at a design luminosity of $10^{34}\,\mathrm{cm}^{-2}\mathrm{s}^{-1}$ is approximately 40 MHz. Besides the limitation of the data readout bandwidth, recording all the information provided by the detectors would lead to a data volume of almost 60 TByte/s. However, only some of the events are interesting enough to be recorded. Therefore, ATLAS uses a two-level trigger system that decides which events to save and which events to discard.

The Level-1 hardware-based trigger (L1) uses a subset of the information provided by the detector components. Using custom electronics, the events are scanned for the presence of high p_T leptons, photons and missing transverse energy, which could indicate the decay of a heavy particle. Furthermore, so called regions-of-interest are defined in which interesting features have been identified. The L1 trigger reduces the event rate to around 100 kHz. The events from the first level trigger are then processed by the software-based high-level trigger (HLT). Using reconstructed detector data within the regions-of-interest, the HLT reduces the event rate to around 1 kHz which is then recorded for permanent storage.

4. The Search for Higgs Boson Pair Production in the $b\bar{b}WW^*$ Channel in the 1 Lepton Final State

In this chapter, the search strategy of the $HH \to b\bar{b}WW^*$ analysis [26] is presented. At first the decay channel targeted in the analysis is discussed. In the next section, the definitions of the objects used in the analysis and their reconstruction from the detector signals are given. Furthermore, a procedure for overlap removal, the event selection and the background estimation is presented.

4.1. Decay channel

The analysis searches for heavy resonances X that decay into two Higgs bosons H. For this the $HH \to b\bar{b}WW^*$ decay channel, where the two Higgs bosons decay into a pair of b quarks and a pair of W bosons, respectively, is targeted. Considering the branching ratios of the Higgs boson from Table 2.2, the overall branching ratio of the $HH \to b\bar{b}WW^*$ decay channel is 25%, which makes it the channel with the second largest branching ratio after the $HH \to b\bar{b}b\bar{b}$ channel. In the analysis only final states with a single lepton are considered, thus, one of the W bosons decays leptonically, while the other W boson decays into two light flavour quarks. The branching ratios for these decays are 10.86 % and 67.41 %, respectively [9].

The unknown mass of the particle X that decays into the two Higgs bosons, determines the topology of the event. For large resonance masses, the resulting Higgs bosons will have a high p_T. Therefore, their decay products will be boosted and close to each other in the lab frame. This boosted topology makes it difficult to reconstruct the individual jets originating from the b or light flavour quarks. Larger jets, so called Track-Assisted Reclustered (TAR) jets, that contain the hadronic decay products of the Higgs and W boson, are therefore used in the analysis, and will be discussed in the next section. The lepton from the leptonically decaying W boson is also highly boosted and usually is part

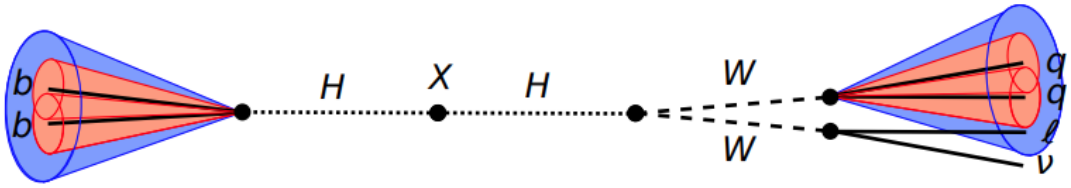

Figure 4.1.: Depiction of the $X \to HH \to b\bar{b}WW^*$ decay channel with a single lepton in the final state in the boosted topology. The heavy resonance X decays into two Higgs boson which decay in turn into a $b\bar{b}$ pair and two oppositely charged W bosons. One of the W bosons decays leptonically while the other one decays into two light flavour quarks.

of the large jet containing the light flavour quarks. A special overlap removal procedure is used to disentangle the lepton from the jet. A depiction of the decay channel in the boosted topology as well as the large jets containing the decay products is given in Figure 4.1.

4.2. Object definitions

In the following section an overview of the definitions of the objects used in the analysis and their reconstruction from the detector signals is given.

Jets

The energy deposits of particles traversing the detector form topological clusters in the calorimeter. Using the anti-k_t algorithm [27], jets are reconstructed from these clusters for a specific radius parameter R. Standard jets are reconstructed using a radius parameter of $R = 0.4$. They are required to have $p_T > 20\,\text{GeV}$ and $|\eta| < 4.5$. The small-R jets, which make up the subjets within the TAR jets, have a radius parameter of $R = 0.2$ and must fulfil $p_T > 15\,\text{GeV}$ and $|\eta| < 2.5$.

Due to the boosted topology of the event, the analysis makes use of Track-Assisted Reclustered (TAR) jets [28], which perform well in dense environments. To construct the TAR jets, small-R jets are clustered into large-R jets with a radius parameter of $R = 1.0$. Subsequently, a trimming procedure is applied, where the small-R subjets with $p_T^{\text{subjet}}/p_T^{\text{jet}} < 0.05$ are removed. After the trimming, tracks are matched to the remaining

small-R jets using ghost-association [29]. To account for missing energy due to neutral hadrons, the p_T^{track} of the tracks is scaled, using the p_T^{subjet} of the subjet it is matched to, according to

$$p_T^{\text{track,new}} = p_T^{\text{track,old}} \times \frac{p_{T,j}^{\text{subjet}}}{\sum\limits_{i \in j} p_{T,i}^{\text{track,old}}},$$

where the variable i denotes the track matched to subjet j. Further requirements on the TAR jets in this analysis are $p_T > 100\,\text{GeV}$ and $|\eta| < 2.0$. To determine the flavour of the quarks from which the jets originated, flavour tagging is performed on variable-R (VR) track jets which are then ghost-associated to the TAR jets. For b-tagging the DLr algorithm [30] with a 77% working point is used. If there is one b-tagged VR track that is ghost-associated to the TAR jet, the TAR jet is called single b-tagged. The TAR jet is double b-tagged if there are two ghost-associated b-tagged VR jets.

Leptons

Electrons are reconstructed by matching energy clusters in the electromagnetic calorimeter to tracks measured in the inner detector. The electron candidates are required to have $p_T > 10\,\text{GeV}$ and $|\eta| < 2.47$. The transition region $1.37 < |\eta| < 1.52$ between the barrel and end-cap of the calorimeter is excluded. Furthermore the electron candidates need to satisfy loose likelihood identification and tight isolation criteria.

Muons are reconstructed by matching a track from the inner detector to a track in the muon spectrometer. Muon candidates are required to have $p_T > 10\,\text{GeV}$ and $|\eta| < 2.5$. Moreover, medium identification and tight isolation criteria need to be satisfied.

In the analysis, tau leptons are only considered if they decay leptonically into an electron or a muon; the hadronically decaying tau leptons are excluded.

Missing transverse energy

The missing transverse energy E_T^{miss} (MET) is defined as the negative vector sum of the p_T of the reconstructed jets and particles. The MET also includes a soft term consisting of tracks not belonging to any of the aforementioned objects.

4.3. Overlap removal

The object reconstruction algorithms of ATLAS run independently of each other. Therefore, some clusters or tracks may be used for the reconstruction of more than one object

and will lead to a double counting of energies. To prevent this, an overlap removal procedure is applied:

(i) An electron is discarded if it shares an inner detector track with a muon. A muon is discarded if it is a calorimeter muon and shares an inner detector track with an electron.

(ii) A jet is discarded and an electron is kept if $\Delta R < 0.2$, where ΔR is the distance between the jet and the electron.
An electron is discarded and the jet is kept if $\Delta R < \min\left(0.4, 0.04 + \frac{10\,\text{GeV}}{p_T^e}\right)$.

(iii) A jet is discarded and a muon is kept if there are less than three tracks in the jet, the muon is ghost-associated to the jet or $\Delta R < 0.2$, where ΔR is the distance between the jet and the muon.
A muon is discarded and the jet is kept if $\Delta R < \min\left(0.4, 0.04 + \frac{10\,\text{GeV}}{p_T^\mu}\right)$.

(iv) A small-R jet is discarded and an electron is kept if $\Delta R < 0.2$, where ΔR is the distance between the small-R jet and the electron.

Due to the boosted topology of the analysis, particles are close to each other when passing through the detector. Therefore, the lepton can end up inside the large-R jet originating from the hadronically decaying W boson. Using standard jets, the overlap removal procedure described above would either reject the lepton and keep the jet or vice versa. Using TAR jets, however, the overlap removal procedure is applied to the small-R subjets that make up the TAR jets. This way subjets, and not the entire jet, overlapping with the lepton are removed, preventing the double counting of energies.

4.4. Event selection

For the $HH \to b\bar{b}WW^*$ single lepton mode to be analysed, only events satisfying the following preselection criteria are considered. Additional cuts on the events passing the preselection are applied to define the signal, validation and control regions used by the analysis. The definitions of the control regions are given in Section 4.5.

Preselection

Only events that pass a single large-R jet trigger and contain one signal lepton, either an electron or a muon, are considered. Furthermore, events are selected that contain at least two TAR jets. The TAR jet closest to the lepton is classified as the hadronically

decaying W boson W_{had}. The $H \to b\bar{b}$ candidate is set to be the TAR jet with the largest p_T that is not the W_{had} candidate. Moreover, the distance between the lepton and the W_{had} candidate is required to satisfy $\Delta R(\ell, W_{\text{had}}) < 1.0$, while for the $H \to b\bar{b}$ candidate $p_T^{H \to b\bar{b}} > 500\,\text{GeV}$ is also required.

Signal regions

For the signal region (SR), events passing the preselection are selected for which the TAR jet of the $H \to b\bar{b}$ candidate is either single or double b-tagged. Events with additional b-tagged jets are rejected. Different signal regions are defined for the lepton channels depending on the number of b-tags of the $H \to b\bar{b}$ candidate and whether its mass falls within a certain percentage of a defined mass window. The definitions of the signal regions are given in Table 4.1.

Table 4.1.: Definitions of the signal regions for the electron and muon channel.

Lepton channel	Signal region
electron	$H \to b\bar{b}$ candidate passes 70% mass window and has $\geq 2b$-tags
muon	$H \to b\bar{b}$ candidate passes 70% mass window and has $1b$-tag
	$H \to b\bar{b}$ candidate passes 70% mass window and has $\geq 2b$-tags
	$H \to b\bar{b}$ candidate fails 70% mass window and has $\geq 2b$-tags

Validation regions

Events in the validation regions (VR) are events passing the preselection for which the TAR jet of the $H \to b\bar{b}$ candidate is either single or double b-tagged. Events with additional b-tagged jets are rejected. Validation regions are defined in a way such that they are close to the signal regions to allow validating the modelling of the backgrounds by comparing to data without introducing a bias and losing too much signal sensitivity. The definitions of the validation regions are given in Table 4.2.

4.5. Background estimation

In the $HH \to b\bar{b}WW^*$ decay channel, the main background contributions originate from $t\bar{t}$, W+jets, diboson, single top and QCD multijet processes. For $t\bar{t}$ processes, two top quarks produced during the collision each decay into a W boson and a b quark, while the single top background contribution arises from the decay of one top quark. The diboson

Table 4.2.: Definitions of the validation regions for the electron and muon channel.

Lepton channel	Validation region
electron	$H \to b\bar{b}$ candidate fails 80% mass window and has 1b-tag
	$H \to b\bar{b}$ candidate fails 80% mass window and has $\geq 2b$-tags
	$H \to b\bar{b}$ candidate passes 70% mass window and has 1b-tag
muon	$H \to b\bar{b}$ candidate fails 80% mass window and has 1b-tag

background originates from the decay of two bosons produced during the collision. Most of these backgrounds are estimated using MC simulation, while a data driven approach is used for the estimation of the QCD background. However, corrections have to be applied to account for the mismodelling of trigger responses, reconstruction, isolation and identification efficiencies. To estimate the correct normalisation for the predicted event yield of the MC modelled background processes, data from dedicated control regions (CR) is used. Control regions are defined in such a way that they are orthogonal to the signal region and that a certain background process is dominant in the event composition. By fitting the simulated distributions to the data, the normalisation factors for the backgrounds can be obtained. The definitions of the control regions for the $t\bar{t}$, W+jets and QCD background processes are given in Table 4.3.

Table 4.3.: Definitions of control regions for the background processes.

Background process	Control region
$t\bar{t}$	2 b-tagged TAR jets, $m_{\text{TAR}}^{W_{\text{had}}} < 20\,\text{GeV}$
W+jets	0 b-tagged TAR jets, $H \to b\bar{b}$ candidate fails 70% mass window, $60\,\text{GeV} < m_T^{W_{\text{lep}}} < 120\,\text{GeV}$
QCD	0 b-tagged TAR jets, $H \to b\bar{b}$ candidate fails 70% mass window, not W+jets

QCD background estimate

The QCD background is the background caused by fake or non-prompt leptons, which are either jets that were incorrectly reconstructed as leptons or leptons that are not originating from the primary vertex. This background is difficult to describe with MC simulation and a data driven approach is used for its estimation.

The QCD background is estimated using the so called matrix method for which two lepton criteria “loose” and “tight” are used. The criteria are combinations of likelihood

identification (LH ID) and isolation requirements given in Table 4.4. The tight leptons are the signal leptons that are used in the analysis.

Table 4.4.: Definitions of the loose and tight criteria used for the QCD background estimation.

Lepton	Loose	Tight
electron	loose LH ID and no isolation	medium LH ID and tight track only isolation
muon	loose ID and no isolation	medium ID and tight track only isolation

Furthermore, the real rate ϵ at which prompt leptons pass the tight criteria, and the fake rate f at which non-prompt leptons pass the tight criteria are used. They are defined as follows

$$\epsilon = \frac{N_{\text{prompt,T}}}{N_{\text{prompt}}} \quad \text{and} \quad f = \frac{N_{\text{QCD},T}}{N_{\text{QCD}}},$$

where N_{prompt} is the number of prompt leptons, N_{QCD} is the number of non-prompt leptons and the index T refers to the number of tight leptons. The real rate ϵ is estimated using MC simulation, while the fake rate f is measured in the QCD CR defined in Table 4.3. The rates can be binned in different quantities, e.g. in the p_T of the lepton or in the ΔR between the lepton and the closest jet to obtain predictions of kinematic distributions for the QCD background.

Using these rates, the number of tight leptons N_T and the number of leptons that pass the loose but not the tight criteria N_{LnT} can be expressed by the following matrix equation

$$\begin{pmatrix} N_T \\ N_{\text{LnT}} \end{pmatrix} = \begin{pmatrix} \epsilon & f \\ 1-\epsilon & 1-f \end{pmatrix} \begin{pmatrix} N_{\text{prompt}} \\ N_{\text{QCD}} \end{pmatrix} . \tag{4.1}$$

Since N_T and N_{LnT} are known, the number of non-prompt leptons can be determined by inverting the matrix in eq. (4.1). To consider signal leptons only, the expression for N_{QCD} is multiplied by the fake rate f. Therefore, the number of non-prompt leptons that pass the tight criteria is given by

$$N_{\text{QCD},T} = \frac{f(\epsilon-1)}{\epsilon-f} N_T + \frac{f\epsilon}{\epsilon-f} N_{\text{LnT}} . \tag{4.2}$$

To estimate the QCD background in the signal region, each data event is weighted by the expression given in eq. (4.2).

5. Systematic Uncertainties and their Impact on Kinematic Distributions

In this chapter an investigation into the systematic uncertainties of the analysis is presented. The systematic uncertainties are relevant for the search sensitivity of the analysis and it is therefore important to quantify their effects.

A systematic uncertainty is a variation in a measurement, that unlike a statistical uncertainty does not vary randomly with each data point. In contrast to statistical uncertainties which scale with $1/\sqrt{N}$, with N being the number of measurements, systematic uncertainties do not have the same behaviour as they arise from imperfect modelling or calibration of the measurement instruments. Therefore, the systematic uncertainties in the analysis can be divided into MC modelling uncertainties and experimental uncertainties related to the detector. The latter are the ones considered in this thesis. These include uncertainties on the electron and muon identification and reconstruction efficiencies, as well as uncertainties on their momentum and energy resolutions. Furthermore, systematic uncertainties on the jet energy scale and jet energy resolution in addition to b-tagging uncertainties are considered.

A selection of systematic uncertainties that have a visible impact on the kinematic distributions considered, is given in Table 5.1. In the table, the names for the systematic uncertainties as used by the analysis and a description is provided. A complete overview of the systematic uncertainties considered in the analysis is given in Table A.1.

In the analysis the systematic uncertainties are applied to the reconstructed objects by the framework[1] being used. This is done once with a shift by $+1\sigma$ which is called the "1up" variation and once with a shift by -1σ called the "1down" variation. These uncertainties on the reconstructed objects will be propagated through the full analysis chain to the final quantities relevant to the analysis.

[1] A brief overview of the framework being used by the analysis is given in Appendix A.1.

Table 5.1.: Examples of systematic uncertainties with a large impact on the kinematic distributions. The full list of systematic uncertainties and their description is given in Table A.1.

Systematic uncertainty	Description
JET_CR_JET_JER_EffectiveNP	jet energy resolution uncertainty (split into components 1 to 7)
JET_CR_JET_EffectiveNP_Mixed	jet energy scale uncertainty (split into components 1 to 3)
JET_CR_JET_Flavor_Composition	jet energy scale uncertainty on samples' flavour composition
JET_CR_JET_Flavor_Response	jet energy scale uncertainty on samples' flavour response
PRW_DATASF	pileup reweighting uncertainty
MET_SoftTrk_ResoPara	missing transverse energy track-based soft term related to longitudinal resolution uncertainty
MUON_ID	muon momentum resolution uncertainty from the inner detector
MUON_MS	muon momentum resolution uncertainty from the muon system

In this thesis, the impact of the systematic uncertainties on the shape of six different kinematic distributions is evaluated. The distributions considered are given in Table 5.2. Furthermore, only kinematic distributions for the signal process with a resonance mass of 2 TeV, the W+jets background and the $t\bar{t}$ background are considered. The W+jets and $t\bar{t}$ backgrounds were chosen because they are the most dominant background processes and the only background samples available so far that have systematic uncertainties included. While the results for the W+jets background process are presented in this thesis, the results for the $t\bar{t}$ background can be found in Appendix A.3. Furthermore, for now jet uncertainties on standard jets are used, also as a proxy for the uncertainties on small-R jets, since these small-R jet uncertainties are not available yet.

Table 5.2.: Overview of the kinematic distributions considered.

Distribution	Description
$m^{HH}_{\text{vis+met}}$	final discriminant, calculated from the mass of the $H \to b\bar{b}$ and W_{had} candidate, the lepton mass and the missing transverse energy
p^{ℓ}_{T}	transverse momentum of the signal lepton
$m^{H\to b\bar{b}}_{\text{TAR}}$	mass of the p_T leading TAR jet, that is not the W_{had} candidate
$m^{W_{\text{had}}}_{\text{TAR}}$	mass of the TAR jet closest to the lepton
E^{miss}_{T}	missing transverse energy
$m^{W_{\text{lep}}}_{T}$	transverse mass calculated from the lepton mass and the missing transverse energy

5.1. Example: Muon momentum resolution uncertainty

In this section, the impact of the systematic uncertainties on the kinematic distributions is presented by considering the muon momentum resolution uncertainty originating from the inner detector (MUON_ID) as an example. Figure 5.1 and Figure 5.2 show the nominal, 1up and 1down distributions for the 2 TeV signal and W+jets background sample, respectively.

The distributions are shown in the signal region defined in Table 4.1 where the $H \to b\bar{b}$ candidate passes the 70% mass window and the corresponding TAR jet is double b-tagged. Furthermore, the inclusive lepton channel is considered, which means that the lepton can be either an electron or a muon, since this signal region is defined for both lepton flavours.

For the signal process, it can be observed that the uncertainty on the muon momentum resolution has very little impact on the $m_{\text{TAR}}^{H\to b\bar{b}}$ distribution, which is the distribution of the mass of the $H \to b\bar{b}$ candidate and therefore peaks around the physical Higgs boson mass at 125 GeV. The effect on the $m_{\text{TAR}}^{W_{\text{had}}}$ distribution is negligible as well. The distribution shows two peaks, one at the physical W boson mass at 80 GeV and one at 35 GeV, which corresponds to the case where the hadronically decaying W boson is off-shell. The largest variations due to the systematic uncertainty can be seen in the p_T^{ℓ} and E_T^{miss} distributions. Therefore, the derived distribution of the transverse mass of the leptonically decaying W boson $m_T^{W_{\text{lep}}}$ is affected as well. Finally, the uncertainty of the muon momentum resolution also impacts the final discriminating distribution $m_{\text{vis+met}}^{HH}$, which is calculated from the mass of the $H \to b\bar{b}$ and W_{had} candidate, the lepton mass and the missing transverse energy. Although it does not describe the total mass m^{HH} of the system due to the missing momentum of the neutrino in the z-direction, the distribution is expected to peak around the resonance mass of 2 TeV, which can be seen in Figure 5.1.

For the W+jets background process, the shape of the distributions seen in Figure 5.2 appears different from the shape of the distributions for the signal process. It can be seen, that the uncertainty on the muon momentum resolution has a large impact on the E_T^{miss} and $m_T^{W_{\text{lep}}}$ distribution, whereas the shape of the $m_{\text{TAR}}^{H\to b\bar{b}}$ and $m_{\text{TAR}}^{W_{\text{had}}}$ distribution is almost not affected by the uncertainty. The relatively large fluctuations can be explained by the fact that for the W+jets background only Monte Carlo samples representing 2017 data were used and therefore low statistics are expected.

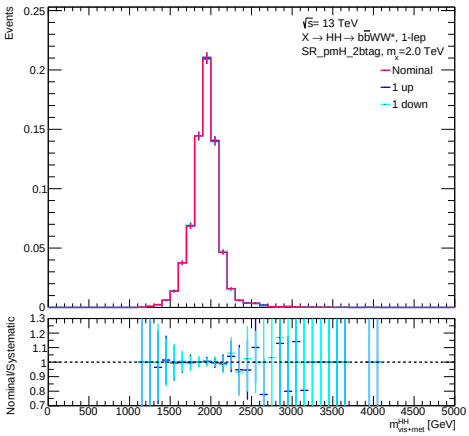

(a) $m^{HH}_{\text{vis+met}}$

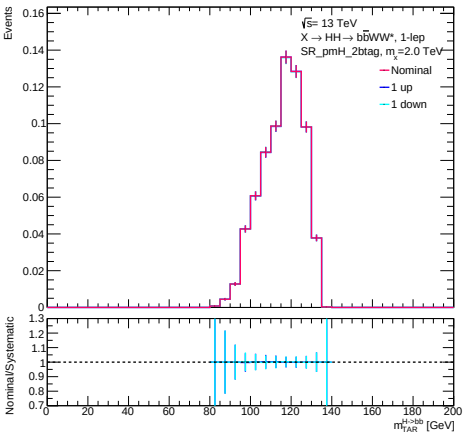

(b) $m^{H\to b\bar{b}}_{\text{TAR}}$

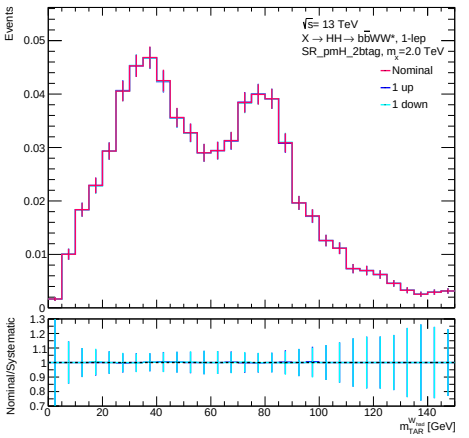

(c) $m^{W_{\text{had}}}_{\text{TAR}}$

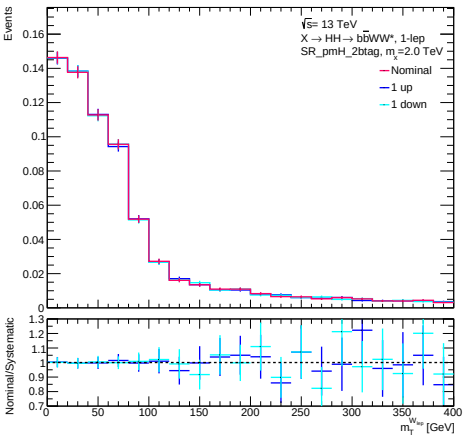

(d) $m^{W_{\text{lep}}}_{T}$

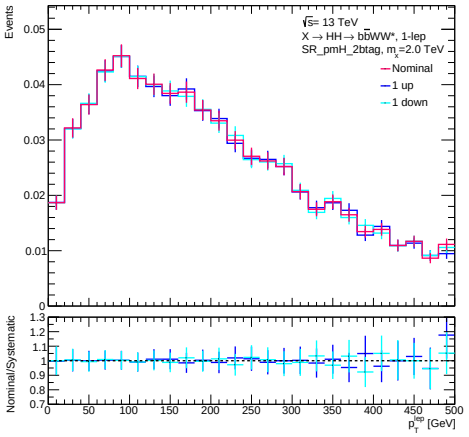

(e) p^{ℓ}_{T}

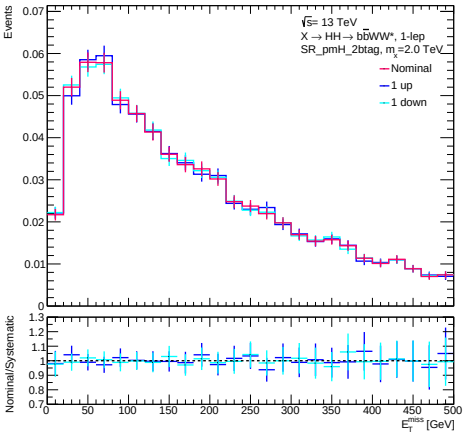

(f) E^{miss}_{T}

Figure 5.1.: Kinematic distributions for the muon momentum resolution systematic uncertainty for the 2 TeV signal sample.

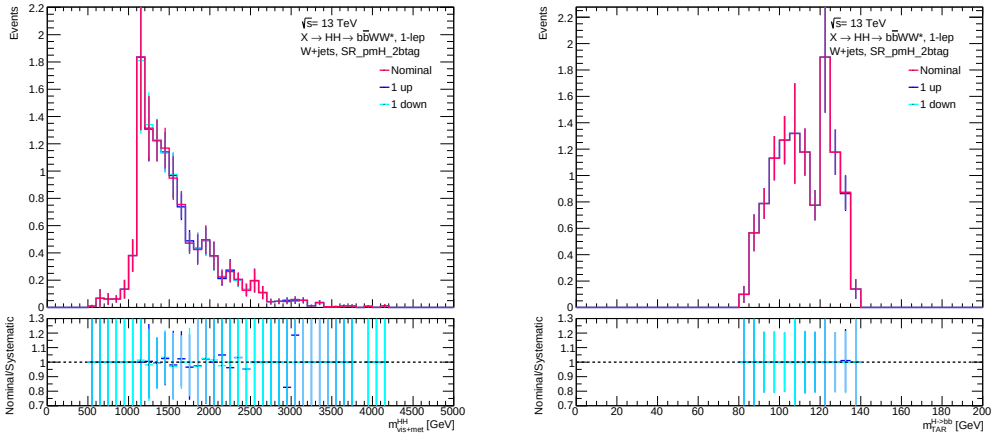

(a) $m^{HH}_{\text{vis+met}}$

(b) $m^{H\to b\bar{b}}_{\text{TAR}}$

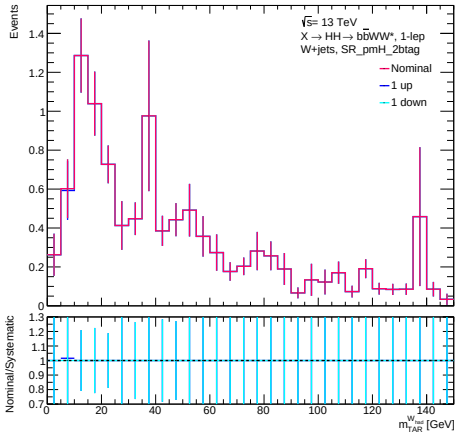

(c) $m^{W_{\text{had}}}_{\text{TAR}}$

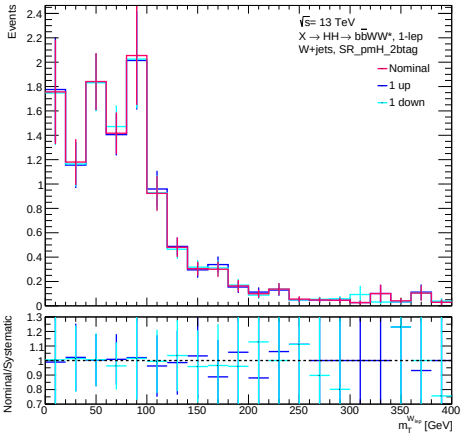

(d) $m^{W_{\text{lep}}}_{T}$

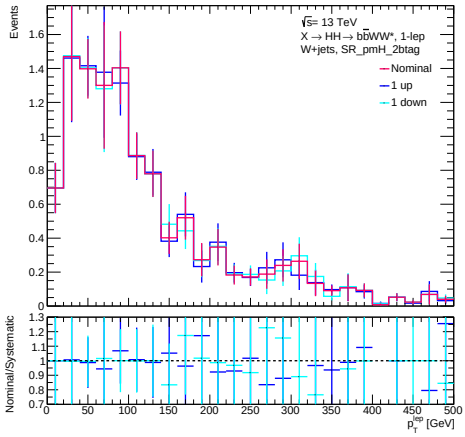

(e) p^{ℓ}_{T}

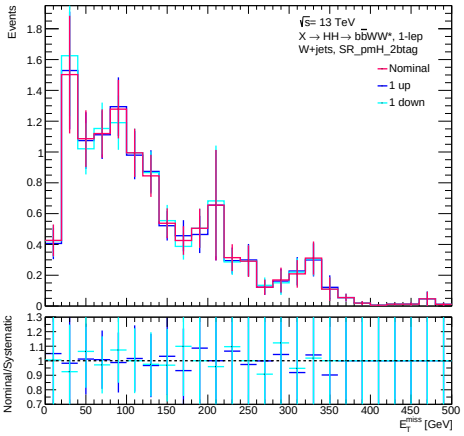

(f) E^{miss}_{T}

Figure 5.2.: Kinematic distributions for the muon momentum resolution systematic uncertainty for the W+jets background sample.

5.2. Example: Jet energy scale flavour composition uncertainty

In this section, the impact of a jet energy scale systematic uncertainty on the kinematic distributions is presented. The uncertainty considered is the uncertainty on the energy scale of standard jets that is caused by the uncertainty on the fraction of gluon and light quark initiated jets of the sample. This uncertainty is henceforth referred to as the jet energy scale flavour composition uncertainty (JET_CR_JET_Flavor_Composition).

Figure 5.3 and Figure 5.4 show the nominal, 1up and 1down distributions for the 2 TeV signal and W+jets background sample respectively. The signal region and lepton channel considered, are the same as in Section 5.1.

For the signal process, the shapes of the distributions resemble the ones described in the previous section. It can be seen that the jet energy scale flavour composition uncertainty causes the largest deviation from the nominal shape in the $m_T^{W_{\text{lep}}}$ and E_T^{miss} distributions. The differences in the E_T^{miss} distribution in turn impact the final discriminating distribution $m_{\text{vis+met}}^{HH}$. The uncertainty appears to have no effect on the p_T^{ℓ}, $m_{\text{TAR}}^{W_{\text{had}}}$ and $m_{\text{TAR}}^{H\to b\bar{b}}$ distributions. The same behaviour can be observed for the distributions of the W+jets background process.

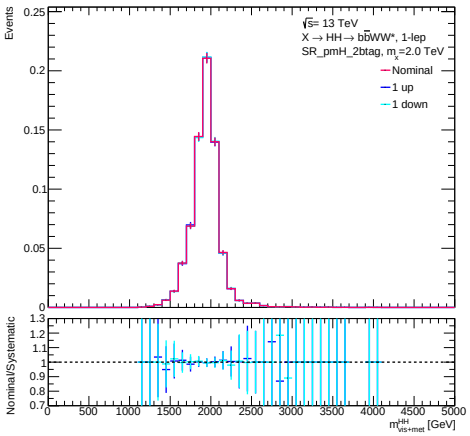

(a) $m^{HH}_{\text{vis+met}}$

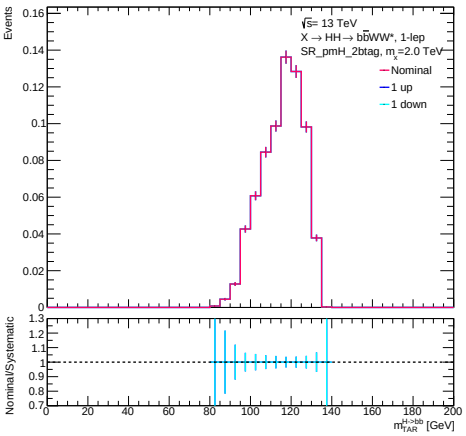

(b) $m^{H\to b\bar{b}}_{\text{TAR}}$

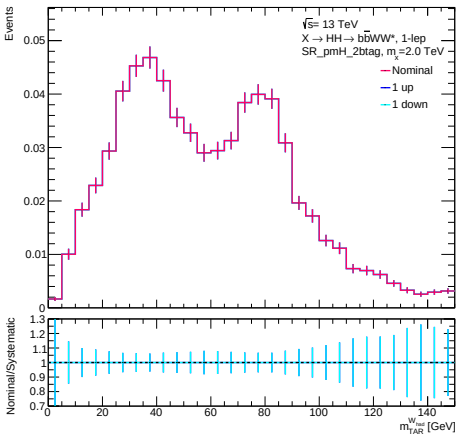

(c) $m^{W_{\text{had}}}_{\text{TAR}}$

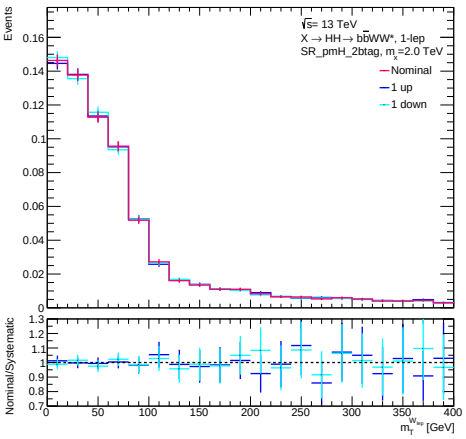

(d) $m^{W_{\text{lep}}}_{T}$

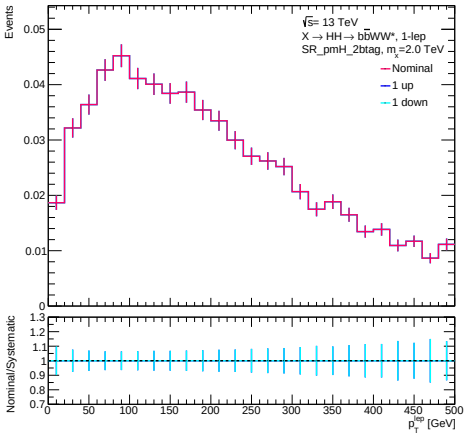

(e) p^{ℓ}_{T}

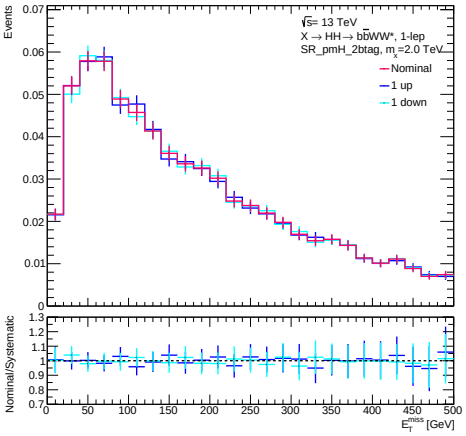

(f) E^{miss}_{T}

Figure 5.3.: Kinematic distributions for the jet energy scale flavour composition systematic uncertainty for the 2 TeV signal sample.

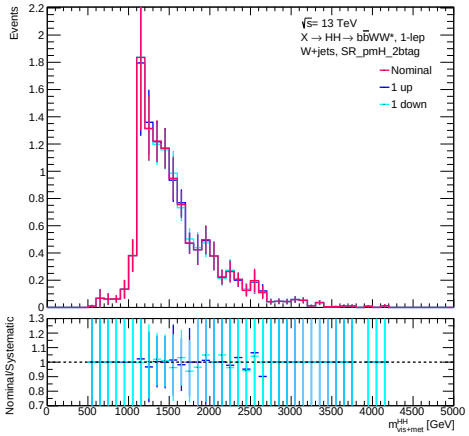

(a) $m^{HH}_{\text{vis+met}}$

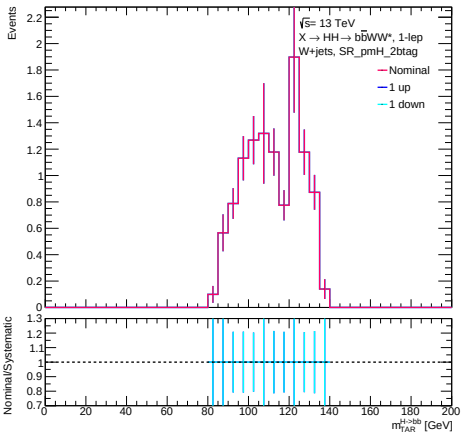

(b) $m^{H\to b\bar{b}}_{\text{TAR}}$

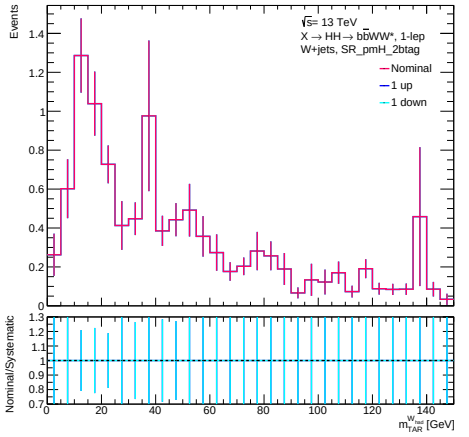

(c) $m^{W_{\text{had}}}_{\text{TAR}}$

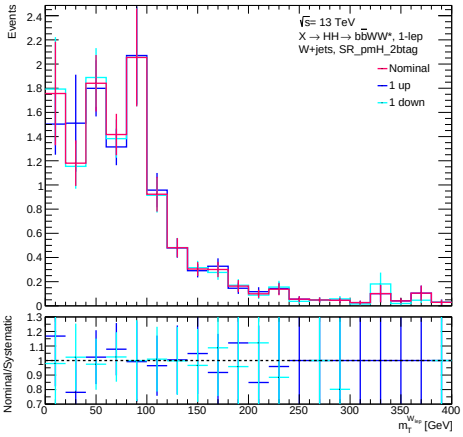

(d) $m^{W_{\text{lep}}}_{T}$

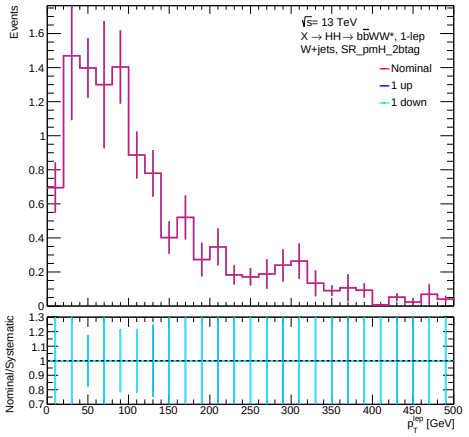

(e) p^{ℓ}_{T}

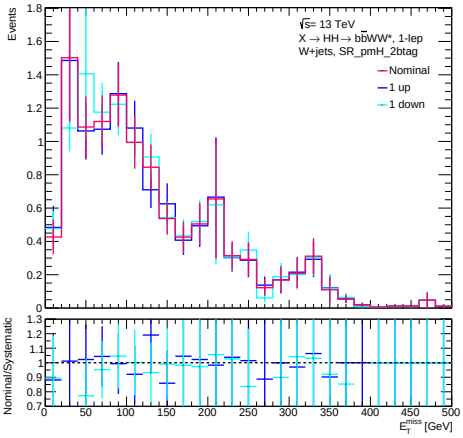

(f) E^{miss}_{T}

Figure 5.4.: Kinematic distributions for the jet energy scale flavour composition systematic uncertainty for the W+jets background sample.

5.3. Quantification of impact

For every distribution, the difference between the nominal and 1up or 1down distribution is quantified by calculating a reduced χ^2_ν value, which is defined as follows

$$\chi^2_\nu = \frac{1}{\nu} \sum_{i=0}^{n} \frac{(O_i - E_i)^2}{\sigma_i^2} \ ,$$

where O_i and E_i are the number of observed and expected events and σ_i is the expected statistical uncertainty in the ith bin of the histograms. In this case the nominal distribution and the distributions with the systematic uncertainties applied are seen as the expected and observed distributions respectively. The number of degrees of freedom, denoted by ν, is given by the number of bins of the histograms. The expectation value of the reduced χ^2_ν that only considers statistical uncertainties will be equal to one and therefore the χ^2_ν values for the systematic uncertainties can be compared to this expectation value.

As an example, the χ^2_ν values for the muon momentum resolution uncertainty from the inner detector for the 1up and 1down variation can be seen in Table 5.3. From this it becomes evident that this specific systematic uncertainty has the largest impact on the $m_T^{W_{\text{lep}}}$ and p_T^ℓ distribution, which can also be seen in Figure 5.1 and Figure 5.2.

Table 5.3.: Reduced χ^2 values for the muon momentum resolution systematic uncertainty from the inner detector.

(a) 2 TeV signal

Distribution	χ^2_ν 1up	χ^2_ν 1down
$m^{HH}_{\text{vis+met}}$	0.0791	0.0269
E_T^{miss}	0.2060	0.1136
p_T^ℓ	0.177	0.1402
$m_T^{W_{\text{lep}}}$	0.3753	0.5355
$m^{H\to b\bar{b}}_{\text{TAR}}$	0.0004	0.0004
$m^{W_{\text{had}}}_{\text{TAR}}$	0.0009	0.0007

(b) W+jets background

Distribution	χ^2_ν 1up	χ^2_ν 1down
$m^{HH}_{\text{vis+met}}$	0.0117	0.0037
E_T^{miss}	0.0196	0.0383
p_T^ℓ	0.1224	0.1472
$m_T^{W_{\text{lep}}}$	0.0461	0.9823
$m^{H\to b\bar{b}}_{\text{TAR}}$	0.0001	0
$m^{W_{\text{had}}}_{\text{TAR}}$	0.0001	0

The χ^2_ν values for the jet energy scale flavour composition systematic uncertainty for the 1up and 1down variation are given in Table 5.4. As can be seen from Figure 5.3 and Figure 5.4 the jet energy scale flavour composition uncertainty has the largest impact on the E_T^{miss} and $m_T^{W_{\text{lep}}}$ distributions.

Table 5.4.: Reduced χ^2 values for the jet energy scale flavour composition systematic uncertainty.

(a) 2 TeV signal

Distribution	χ^2_ν 1up	χ^2_ν 1down
$m^{HH}_{\text{vis+met}}$	0.0176	0.0126
E_T^{miss}	0.1761	0.1084
p_T^{ℓ}	0	0
$m_T^{W_{\text{lep}}}$	0.288	0.2636
$m^{H\to b\bar{b}}_{\text{TAR}}$	0	0
$m^{W_{\text{had}}}_{\text{TAR}}$	0	0

(b) W+jets background

Distribution	χ^2_ν 1up	χ^2_ν 1down
$m^{HH}_{\text{vis+met}}$	0.0038	0.0091
E_T^{miss}	0.11	0.3002
p_T^{ℓ}	0	0
$m_T^{W_{\text{lep}}}$	0.2274	0.2552
$m^{H\to b\bar{b}}_{\text{TAR}}$	0	0
$m^{W_{\text{had}}}_{\text{TAR}}$	0	0

Using the calculated χ^2_ν values for the 1up and 1down variation the systematic uncertainties can be ranked according to their impact on a certain distribution. The ten systematic uncertainties with the largest χ^2_ν values for the 1up and 1down variation of the final discriminating distribution $m^{HH}_{\text{vis+met}}$ for the 2 TeV signal and W+jets background sample are shown in Table 5.5. It becomes clear, that the systematic uncertainty having the largest impact on the final discriminant for the signal process is the uncertainty on the jet energy resolution, while the uncertainty of the pileup reweighting has the largest impact on the discriminant distribution for the W+jets background process. The $m^{HH}_{\text{vis+met}}$ distributions for these two systematic uncertainties are given in Figure 5.5. The complete rankings of all the systematic uncertainties for the 2 TeV signal sample and the W+jets background sample for the $m^{HH}_{\text{vis+met}}$ discriminant distribution are given in Tables A.2 to A.5.

Table 5.5.: Systematic uncertainties with the largest χ^2_ν values for the 1up and 1down variation of the final discriminating distribution $m^{HH}_{\text{vis+met}}$ for the 2 TeV signal and W+jets background sample.

(a) 2 TeV signal 1up

Systematic uncertainty	χ^2_ν 1up
jet energy resolution uncertainty (2)	0.2508
jet energy resolution uncertainty (3)	0.1688
jet energy resolution uncertainty (1)	0.1264
jet energy resolution uncertainty (7)	0.1162
jet energy resolution uncertainty (5)	0.0885
pileup reweighting uncertainty	0.0863
muon momentum resolution uncertainty (ID)	0.0791
jet energy resolution uncertainty (4)	0.0693
jet energy scale uncertainty (flavour response)	0.0614
jet energy scale uncertainty (mixed 1)	0.0615

(b) 2 TeV signal 1down

Systematic uncertainty	χ^2_ν 1down
jet energy resolution uncertainty (2)	0.2508
jet energy resolution uncertainty (3)	0.1688
jet energy resolution uncertainty (1)	0.1264
jet energy resolution uncertainty (7)	0.1162
jet energy scale uncertainty (mixed 1)	0.0946
jet energy resolution uncertainty (5)	0.0885
jet energy resolution uncertainty (4)	0.0693
jet energy scale uncertainty (flavour response)	0.0584
jet energy resolution uncertainty (6)	0.0533
pileup reweighting uncertainty	0.0315

(c) W+jets background 1up

Systematic uncertainty	χ^2_ν 1up
pileup reweighting uncertainty	0.3253
jet energy resolution uncertainty (3)	0.0504
jet energy resolution uncertainty (4)	0.0498
jet energy resolution uncertainty (2)	0.0453
jet energy resolution uncertainty (7)	0.0444
jet energy resolution uncertainty (5)	0.0434
jet energy resolution uncertainty (1)	0.0415
jet energy resolution uncertainty (6)	0.0313
MET (soft term longitudinal resolution)	0.0238
jet energy scale uncertainty (flavour response)	0.02

(d) W+jets background 1down

Systematic uncertainty	χ^2_ν 1down
pileup reweighting uncertainty	0.1348
jet energy resolution uncertainty (3)	0.0504
jet energy resolution uncertainty (4)	0.0498
jet energy resolution uncertainty (2)	0.0453
jet energy resolution uncertainty (7)	0.0444
jet energy resolution uncertainty (5)	0.0434
jet energy resolution uncertainty (1)	0.0415
jet energy resolution uncertainty (6)	0.0313
jet energy scale uncertainty (flavour response)	0.0151
jet energy scale uncertainty (flavour composition)	0.0091

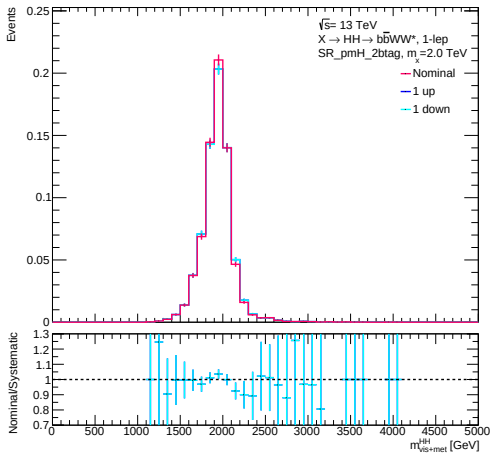

(a) jet energy resolution uncertainty (2)

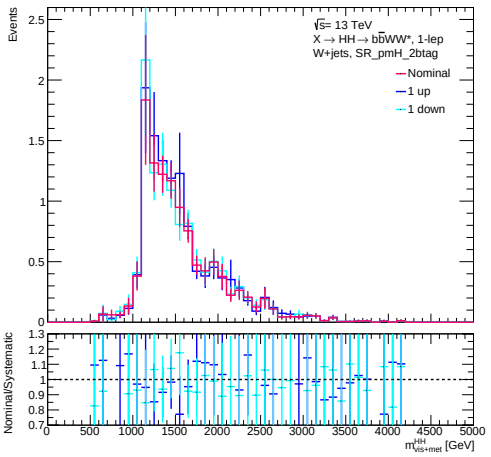

(b) pileup reweighting uncertainty

Figure 5.5.: Final discriminant distribution $m^{HH}_{\text{vis+met}}$ for the systematic uncertainties with the largest impact for the 2 TeV signal process (a) and the W+jets background process (b).

6. Non-closure Uncertainty of the QCD Background Estimate

The aim of the second part of this bachelor thesis is to derive a non-closure uncertainty for the QCD background estimated by the matrix method. As described in Section 4.5, the real and fake rates, ϵ and f used to estimate the QCD background can be binned in different variables. An overview of the considered binning variables, and their description is given in Table 6.1.

Table 6.1.: Overview of the quantities in which the real and fake rate are binned.

Binning quantity	Description
$m_{\text{TAR}}^{W_{\text{had}}}$	mass of the TAR jet closest to the lepton
$p_T^{W_{\text{had}}}$	transverse momentum of the TAR jet closest to the lepton
$\Delta R(\ell, W_{\text{had}})$	distance between the lepton and the W_{had} candidate
η^{ℓ}	η of the signal lepton
$p_T^{H\to b\bar{b}}$	transverse momentum of the p_T leading TAR jet, that is not the W_{had} candidate
E_T^{miss}	missing transverse energy
$m_{\text{vis+met}}^{HH}$	final discriminant, calculated from the mass of the $H \to b\bar{b}$ and W_{had} candidate, the lepton mass and the missing transverse energy
p_T^{ℓ}	transverse momentum of the signal lepton

The modelling of the QCD background varies depending on the binning used for the rates. This can be seen in Figure 6.1 which shows the discriminating distribution $m_{\text{vis+met}}^{HH}$ for the rates binned in $m_{\text{vis+met}}^{HH}$ and the rates binned in $p_T^{H\to b\bar{b}}$. The distributions are shown for the electron channel in the validation region defined in Table 4.2 where the $H \to b\bar{b}$ candidate fails the 80% mass window and has a single b-tag. It can be seen that if the rates are binned in $m_{\text{vis+met}}^{HH}$, the modelling of the QCD background for the $m_{\text{vis+met}}^{HH}$ distribution performs better than if the rates are being binned in $p_T^{H\to b\bar{b}}$.

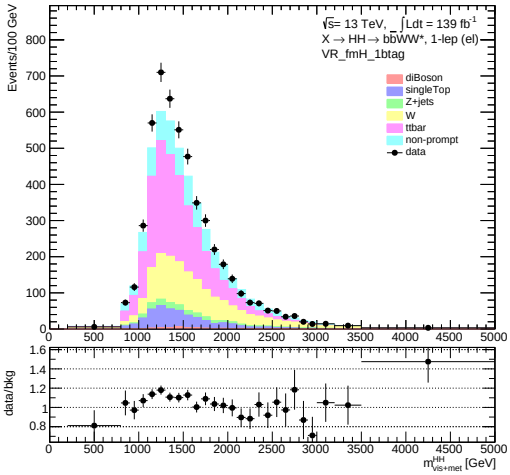

(a) for rates binned in $m^{HH}_{\text{vis+met}}$

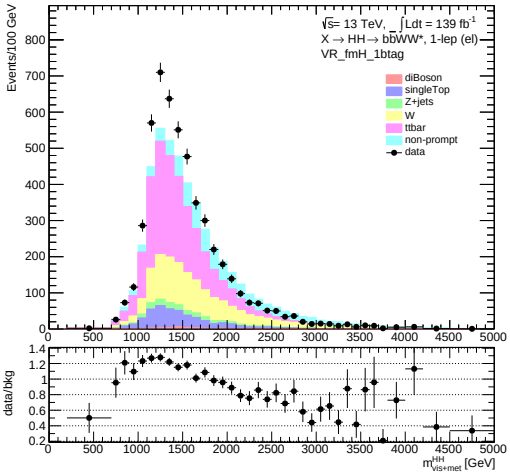

(b) for rates binned in $p_T^{H\to b\bar{b}}$

Figure 6.1.: Distribution of the final discriminant $m^{HH}_{\text{vis+met}}$ for the different backgrounds and data. Shown is the validation region for the electron channel where the $H \to b\bar{b}$ candidate fails the 80% mass window and has a single b-tag. The QCD background is estimated by (a) binning the rates ϵ and f in $m^{HH}_{\text{vis+met}}$ and (b) by binning the rates in $p_T^{H\to b\bar{b}}$.

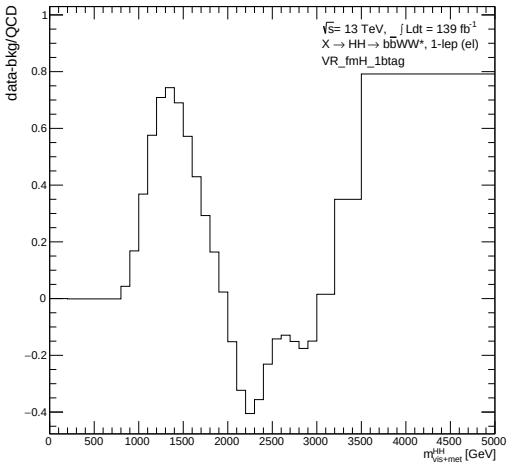

(a) for rates binned in $m^{HH}_{\text{vis+met}}$

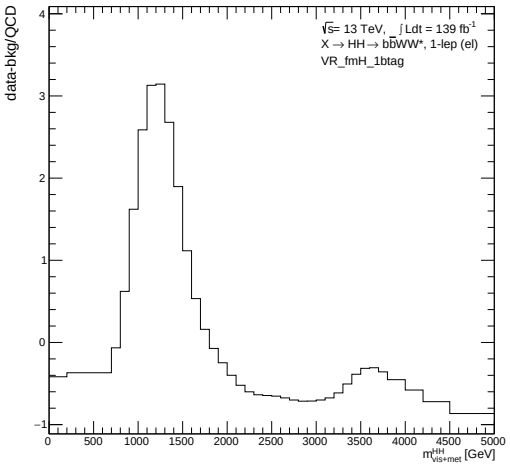

(b) for rates binned in $p_T^{H\to b\bar{b}}$

Figure 6.2.: Difference between data and background distributions for the final discriminant $m^{HH}_{\text{vis+met}}$ relative to the QCD estimate in the electron channel. The QCD background is estimated by (a) binning the rates ϵ and f in $m^{HH}_{\text{vis+met}}$ and (b) by binning the rates $p_T^{H\to b\bar{b}}$. Moreover, a smoothing procedure has been applied to the histograms.

This non-closure is assumed to be due to imperfections in the QCD estimate and an uncertainty to cover this is derived. To determine the uncertainty, the difference histograms describing the difference $\frac{N_{\text{data}}-N_{\text{bkgd}}}{N_{\text{QCD}}}$ between the data and background relative to the QCD estimate are considered. To remove large fluctuations in some of the bins resulting from small event yields in the QCD estimates, the histograms for the distributions are rebinned to ensure that each bin contains a minimum of five predicted QCD events. Moreover, a smoothing procedure is applied to the bin contents of the histograms. The difference histograms for the $m^{HH}_{\text{vis+met}}$ discriminating distribution for the rates binned in $m^{HH}_{\text{vis+met}}$ and for the rates binned in $p_T^{H\to b\bar{b}}$ can be seen in Figure 6.2.

The non-closure uncertainty of the QCD background estimation is derived in two different ways. The uncertainty of the estimation method as well as the uncertainty of the final discriminant distribution $m^{HH}_{\text{vis+met}}$ are obtained. Eventually, as final uncertainty for the QCD background estimate the uncertainty of the $m^{HH}_{\text{vis+met}}$ distribution is planned to be used by the analysis. The uncertainty of the estimation method is used as a cross-check.

6.1. Non-closure uncertainty of the estimation method

The assumption of the estimation method for the QCD background is that the distribution of the quantity in which the rates are being binned, is well modelled. Therefore, to determine the uncertainty on the estimation method, the different binning variables as given in Table 6.1 are chosen and for each the distribution in the corresponding variable is investigated. For example for the binning in $m^{W_{\text{had}}}_{\text{TAR}}$ the $m^{W_{\text{had}}}_{\text{TAR}}$ distribution is analysed. For each of the distributions, the difference histogram is obtained and the maximum difference value is taken. The difference histograms of the distributions for the electron and muon channel are given in Figure 6.3 and 6.4 and Figure 6.5 and 6.6 respectively.

It can be seen from the plots that taking the maximum max $\left(\frac{N_{\text{data}}-N_{\text{bkgd}}}{N_{\text{QCD}}}\right)$ of the difference values leads to very high uncertainties especially in the muon channel, with the high values mostly being driven by bins in the tails of the distributions. There may be ways to prevent the values from being driven by these bins, however, this is beyond the scope of this thesis. In addition, the uncertainties derived by this method are not planned to be used as final uncertainties by the analysis, but instead will be used as a cross-check.

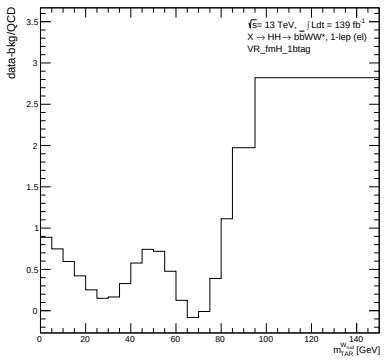

(a) for rates binned in $m_{\mathrm{TAR}}^{W_{\mathrm{had}}}$

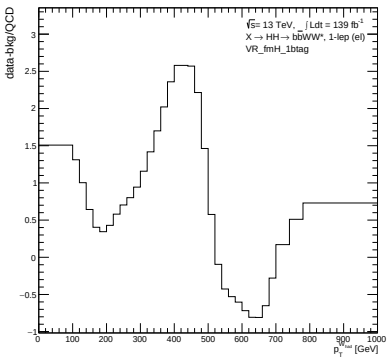

(b) for rates binned in $p_T^{W_{\mathrm{had}}}$

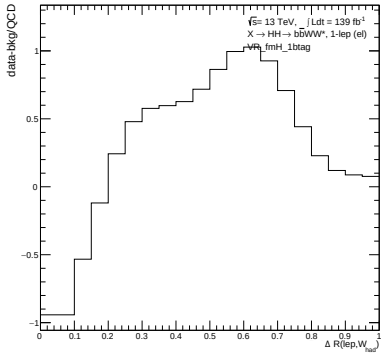

(c) for rates binned in $\Delta R(\ell, W_{\mathrm{had}})$

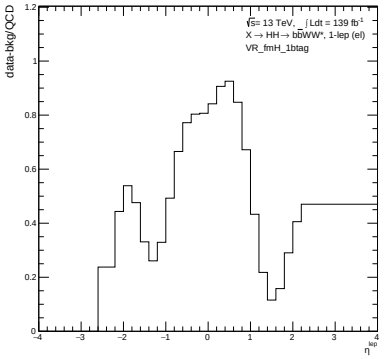

(d) for rates binned in η^{ℓ}

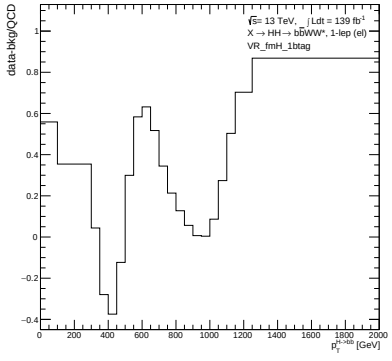

(e) for rates binned in $p_T^{H\to b\bar{b}}$

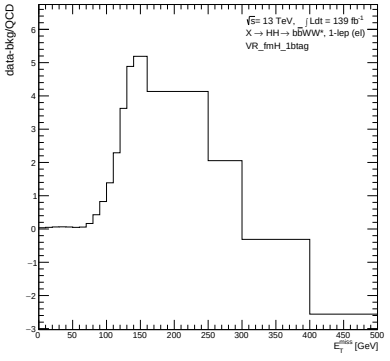

(f) for rates binned in E_T^{miss}

Figure 6.3.: Difference histograms of the electron channel for the quantities that correspond to the rate binning being used.

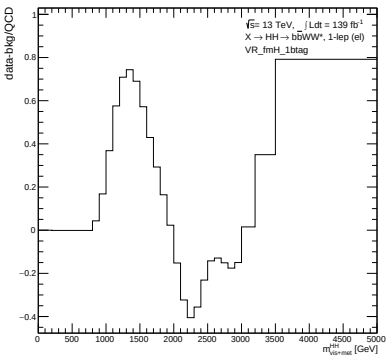

(a) for rates binned in $m^{HH}_{\mathrm{vis+met}}$

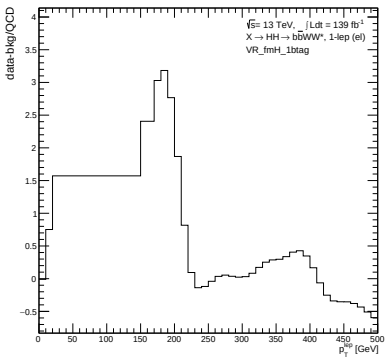

(b) for rates binned in p^{ℓ}_{T}

Figure 6.4.: Difference histograms of the electron channel for the quantities that correspond to the rate binning being used.

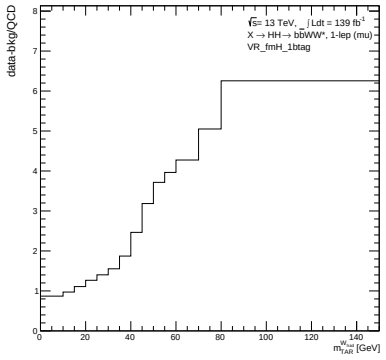

(a) for rates binned in $m^{W_{\mathrm{had}}}_{\mathrm{TAR}}$

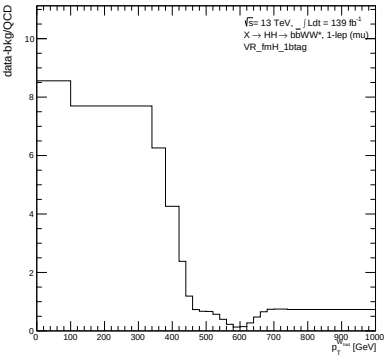

(b) for rates binned in $p^{W_{\mathrm{had}}}_{T}$

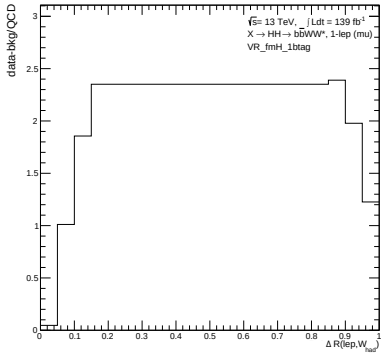

(c) for rates binned in $\Delta R(\ell, W_{\mathrm{had}})$

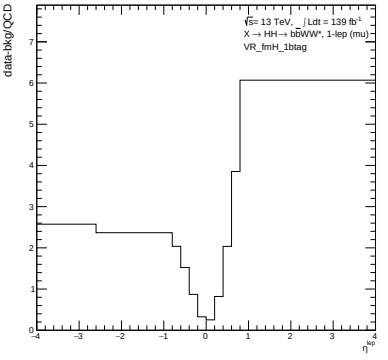

(d) for rates binned in η^{ℓ}

Figure 6.5.: Difference histograms of the muon channel for the quantities that correspond to the rate binning being used.

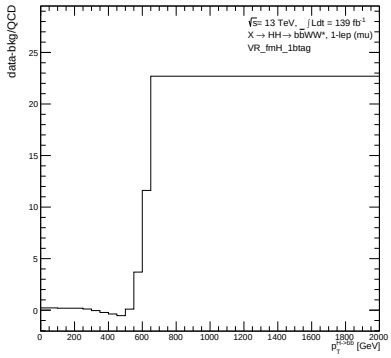

(a) for rates binned in $p_T^{H\to b\bar{b}}$

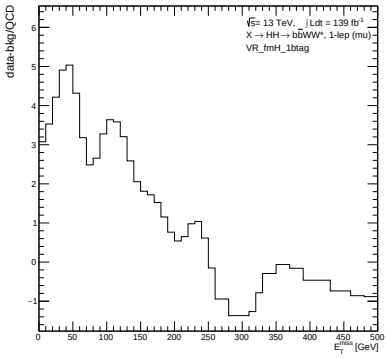

(b) for rates binned in E_T^{miss}

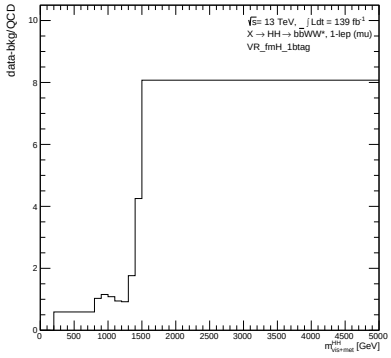

(c) for rates binned in $m_{\text{vis+met}}^{HH}$

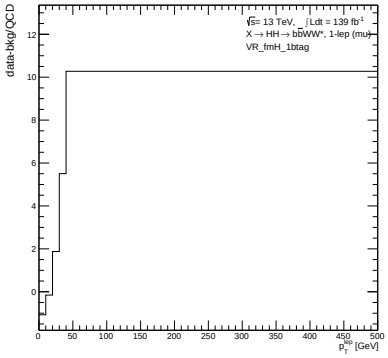

(d) for rates binned in p_T^{ℓ}

Figure 6.6.: Difference histograms of the muon channel for the quantities that correspond to the rate binning being used.

6.2. Non-closure uncertainty of the discriminating distribution

To determine the non-closure shape uncertainty for the final discriminating distribution $m_{\text{vis+met}}^{HH}$, the QCD background is estimated by binning the rates in $m_{\text{TAR}}^{W_{\text{had}}}$, $p_T^{W_{\text{had}}}$, $\Delta R(\ell, W_{\text{had}})$, η^{ℓ} and p_T^{ℓ}.

For each of these QCD estimates the $m_{\text{vis+met}}^{HH}$ distribution is considered and the difference histogram obtained. An overlay of these difference histograms for the $m_{\text{vis+met}}^{HH}$ discriminating distributions for the different QCD estimates is shown in Figure 6.7. For each bin the absolute of the difference values that is larger than 80% of the remaining values is stored in a final difference histogram, which is outlined by the red dotted line in Figure 6.7. The percentage cut was chosen to ensure that the uncertainty is not driven solely by a single binning variable. The method described here, will not be the final approach used by the analysis, but rather serves as a proof of concept.

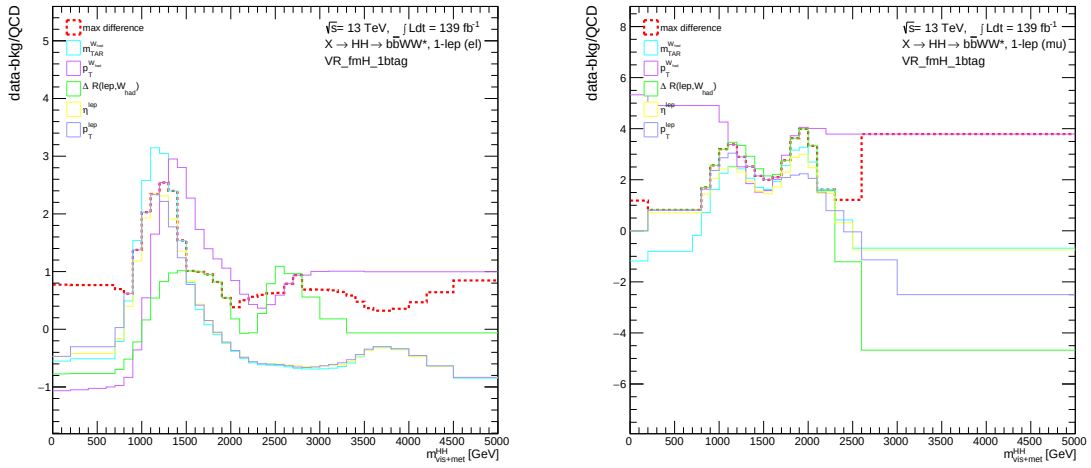

(a) electron ***(b)*** muon

Figure 6.7.: Overlay of the difference histograms for the discriminating $m_{\text{vis+met}}^{HH}$ distribution for the different QCD estimates. The red dotted line outlines the absolute maximum difference with 80% of the values included.

Similar to the approach described in the previous section, the obtained uncertainties are quite large. A possible way to reduce the uncertainties is to consider binning the rates in more basic quantities such as p_T^{ℓ} and $\Delta R(\ell, W_{\text{had}})$ or to consider a 2D binning of the rates in both of these quantities. This is beyond the scope of this thesis, but it is planned to be implemented by the analysis to obtain the final shape uncertainty for the $m_{\text{vis+met}}^{HH}$ discriminating distribution.

7. Conclusion

In this Bachelor's thesis, an investigation into the experimental systematic uncertainties of the $HH \to b\bar{b}WW^*$ boosted analysis with a single lepton in the final state was conducted. The analysis searches for resonant Higgs boson pair production, the detection of which might be possible at the current LHC. The cross section for the non-resonant production on the other hand, is expected to be very small, making detection unlikely at the moment. The final goal of the analysis is to determine upper limits on the cross section of the resonant Higgs boson pair production. These upper limits will be affected by statistical as well as systematic uncertainties, such as the uncertainty of the QCD background estimate. A good estimation of which is therefore necessary for the search sensitivity.

Table 7.1.: Systematic uncertainties with the largest impact for each of the considered kinematic distributions and samples.

(a) 2 TeV signal

Distribution	1up variation	1down variation
$m_{\text{vis+met}}^{HH}$	jet energy resolution uncertainty (2)	jet energy resolution uncertainty (2)
E_T^{miss}	jet energy resolution uncertainty (7)	jet energy scale uncertainty (mixed 1)
$m_T^{W_{\text{lep}}}$	jet energy resolution uncertainty (5)	jet energy resolution uncertainty (5)
$m_{\text{TAR}}^{H\to b\bar{b}}$	pileup reweighting uncertainty	pileup reweighting uncertainty
$m_{\text{TAR}}^{W_{\text{had}}}$	pileup reweighting uncertainty	pileup reweighting uncertainty
p_T^{ℓ}	muon momentum resolution uncertainty (ID)	muon momentum resolution uncertainty (ID)

(b) W+jets background

Distribution	1up variation	1down variation
$m_{\text{vis+met}}^{HH}$	pileup reweighting uncertainty	pileup reweighting uncertainty
E_T^{miss}	pileup reweighting uncertainty	jet energy resolution uncertainty (1)
$m_T^{W_{\text{lep}}}$	pileup reweighting uncertainty	jet energy scale uncertainty (pileup)
$m_{\text{TAR}}^{H\to b\bar{b}}$	pileup reweighting uncertainty	pileup reweighting uncertainty
$m_{\text{TAR}}^{W_{\text{had}}}$	pileup reweighting uncertainty	pileup reweighting uncertainty
p_T^{ℓ}	pileup reweighting uncertainty	pileup reweighting uncertainty

In the first part of the thesis, the impact of the systematic uncertainties on a selected set of kinematic distributions was visualised in plots and quantified by obtaining χ^2_ν values for the 1up and 1down variations. With these χ^2_ν values, the systematic uncertainties

were ranked according to their impact on various distributions. The systematic uncertainties with the largest impact are given in Table 7.1 for the 2 TeV signal and W+jets background sample respectively. It can be seen that for the 2 TeV signal sample, the final discriminating distribution $m^{HH}_{\text{vis+met}}$ is impacted mostly by the uncertainty on the jet energy resolution, whereas for the W+jets sample, the pileup reweighting uncertainty has the largest effect. Overall, for the W+jets background the pileup reweighting uncertainty has the largest impact on almost all distributions considered. For the $t\bar{t}$ background both the pileup reweighting uncertainty and the uncertainty of the jet energy resolution have the largest effect on the discriminating distribution $m^{HH}_{\text{vis+met}}$.

In the second part of the thesis a non-closure uncertainty for the QCD background estimate was derived, by considering two different approaches.

The first approach determined the uncertainty of the estimation method itself, by considering the differences in the distributions that correspond to the binning of the rates being used for the QCD estimate. For each distribution the maximum difference value was taken which led to very high uncertainties especially in the muon channel. However, the uncertainty of the estimation method will not be used as final uncertainty for the QCD background by the analysis.

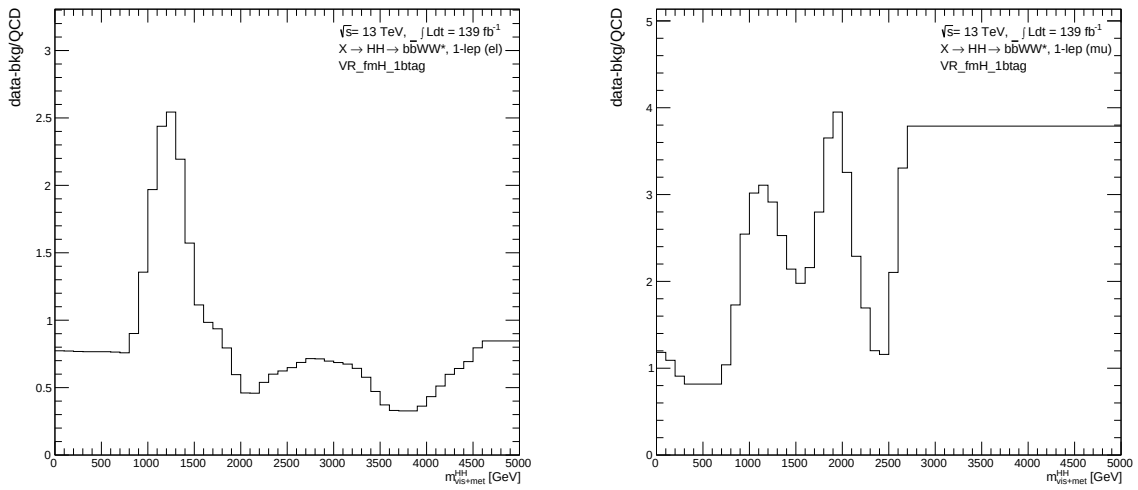

(a) electron ***(b)*** muon

Figure 7.1.: Final difference histograms for the $m^{HH}_{\text{vis+met}}$ discriminating distribution with 80% of the difference values for the different binning quantities included.

The second approach determines the uncertainty of the discriminating $m^{HH}_{\text{vis+met}}$ distribution. For a selected set of QCD estimates, the difference histograms of the $m^{HH}_{\text{vis+met}}$

distribution are obtained. For each bin of the $m^{HH}_{\text{vis+met}}$ distribution, the value from the difference histograms is chosen that is larger than 80% of the other values to obtain the shape uncertainty shown in Figure 7.1 for the final discriminating $m^{HH}_{\text{vis+met}}$ distribution. As discussed in Section 6.2 the resulting uncertainties are large, however, they could be improved upon by considering different binnings of the rates.

With the commissioning of the High-Luminosity Large Hadron Collider (HL-LHC) [31] around 2027, the luminosity is expected to increase to $3000\,\text{fb}^{-1}$ after many years. Consequently, there will be a considerably higher amount of data available, making future analyses more sensitive to non-resonant as well as resonant Higgs boson pair production and other studies regarding physics beyond the Standard Model.

A. Appendix

A.1. CxAOD Framework

The simulated MC samples and the data signals coming from the ATLAS detector are processed by reconstruction algorithms. The algorithms produce so called xAOD files that contain the event data. The xAODs are too large to analyse directly and are therefore reduced further to DxAODs according to the needs of the physics group. The CxAOD-Framework used by the analysis consists of two main parts. The CxAODMaker takes the DxAODs as inputs, reconstructs the TAR jets and applies the systematic variations to the objects. The resulting CxAOD files are then further processed by the CxAODReader which applies additional selections and creates the histograms and trees containing the kinematic distributions of interest.

A.2. Tables

Table A.1.: Overview of the experimental systematic uncertainties.

Systematic Uncertainty	Description
	Electrons
EG_RESOLUTION_ALL	energy resolution uncertainty
EG_SCALE_ALL	energy scale uncertainty
EL_EFF_ID_TOTAL_1NPCOR_PLUS_UNCOR	identification efficiency uncertainty
EL_EFF_Iso_TOTAL_1NPCOR_PLUS_UNCOR	isolation efficiency uncertainty
EL_EFF_Reco_TOTAL_1NPCOR_PLUS_UNCOR	reconstruction efficiency uncertainty
EL_EFF_Trigger_TOTAL_1NPCOR_PLUS_UNCOR	trigger efficiency uncertainty
	Muons
MUON_SCALE	momentum scale uncertainty
MUON_ID	momentum resolution uncertainty from the inner detector
MUON_MS	momentum resolution uncertainty from the muon system
MUON_SAGITTA_RHO MUON_SAGITTA_RESBIAS	charge dependent momentum scale uncertainty
MUON_EFF_ISO_STAT MUON_EFF_ISO_SYS	isolation efficiency uncertainty
MUON_EFF_RECO_STAT MUON_EFF_RECO_SYS	reconstruction and identification efficiency uncertainty for $p_T > 15\,\text{GeV}$
MUON_EFF_RECO_STAT_LOWPT MUON_EFF_RECO_SYS_LOWPT	reconstruction and identification efficiency uncertainty for $p_T < 15\,\text{GeV}$
MUON_EFF_TTVA_STAT MUON_EFF_TTVA_SYS	track-to-vertex association efficiency uncertainty
	Small-R jets
JET_CR_JET_BJES_Response	energy scale uncertainty on b-jets
JET_CR_JET_EffectiveNP_Detector (1 to 2) JET_CR_JET_EffectiveNP_Mixed (1 to 3) JET_CR_JET_EffectiveNP_Modelling (1 to 4) JET_CR_JET_EffectiveNP_Statistical (1 to 6) JET_CR_JET_EtaIntercalibration_Modelling	energy scale uncertainty
JET_CR_JET_EtaIntercalibration_NonClosure_highE JET_CR_JET_EtaIntercalibration_NonClosure_negEta JET_CR_JET_EtaIntercalibration_NonClosure_posEta JET_CR_JET_EtaIntercalibration_TotalStat	energy scale uncertainty on eta-intercalibration
JET_CR_JET_Flavor_Composition	energy scale uncertainty on samples' flavour composition
JET_CR_JET_Flavor_Response	energy scale uncertainty on samples' flavour response
JET_CR_JET_JER_DataVsMC	energy resolution uncertainty
JET_CR_JET_JER_EffectiveNP_1 JET_CR_JET_JER_EffectiveNP_2 JET_CR_JET_JER_EffectiveNP_3 JET_CR_JET_JER_EffectiveNP_4 JET_CR_JET_JER_EffectiveNP_5 JET_CR_JET_JER_EffectiveNP_6 JET_CR_JET_JER_EffectiveNP_7restTerm	energy resolution uncertainty
JET_CR_JET_Pileup_OffsetMu JET_CR_JET_Pileup_OffsetNPV JET_CR_JET_Pileup_PtTerm JET_CR_JET_Pileup_RhoTopology	energy scale uncertainty on pile-up
JET_CR_JET_SingleParticle_HighPt	energy scale uncertainty from the behaviour of high-p_T jets
JET_JvtEfficiency	jet vertex tagger efficiency
	MET
MET_JetTrk_ScaleDown MET_JetTrk_ScaleUp	track-based MET scale uncertainty due to tracks in the jets
MET_SoftTrk_ResoPara	track-based soft term related to longitudinal resolution uncertainty
MET_SoftTrk_ResoPerp	track-based soft term related to transverse resolution uncertainty
MET_SoftTrk_ScaleDown MET_SoftTrk_ScaleUp	track-based soft term related to longitudinal scale uncertainty
	Tracks (not included in this thesis)
TRK_BIAS_D0_WM	d_0 residual alignment tracking uncertainty
TRK_BIAS_Z0_WM	z_0 residual alignment uncertainty

continued on next page

Table A.1 – continued from previous page

Systematic Uncertainty	**Description**
TRK_BIAS_QOVERP_SAGITTA_WM	p_T residual alignment tracking uncertainty
TRK_EFF_LOOSE_GLOBAL	tracking efficiency uncertainty
TRK_EFF_LOOSE_TIDE	tracking efficiency uncertainty in dense environments
TRK_FAKE_RATE_LOOSE	tracking uncertainty on fake rate
TRK_FAKE_RATE_LOOSE_TIDE	tracking uncertainty on fake rate in dense environments
	b-Tagging
FT_EFF_Eigen_Light	b-tagging efficiency uncertainty
FT_EFF_Eigen_C	5 components for light jets, 4 for c jets and 3 for b jets
FT_EFF_Eigen_B	
FT_EFF_extrapolation	b-tagging efficiency uncertainty on the extrapolation on high p_T jets
FT_EFF_extrapolation_from_charm	b-tagging efficiency uncertainty on tau jets
all for AntiKtVR30Rmax4Rmin02TrackJets_BTagging201903	
Additional experimental uncertainties	
PRW_DATASF	pileup reweighting uncertainty
Luminosity	uncertainty on the total integrated luminosity

Table A.2.: Ranking of the systematic uncertainties for the 1up variation of the $m_{\text{vis+met}}^{HH}$ discriminating distribution for the 2 TeV signal sample.

Systematic	χ^2 1up
JET_CR_JET_JER_EffectiveNP_2	0.250758
JET_CR_JET_JER_EffectiveNP_3	0.168757
JET_CR_JET_JER_EffectiveNP_1	0.1264
JET_CR_JET_JER_EffectiveNP_7restTerm	0.116226
JET_CR_JET_JER_EffectiveNP_5	0.0885367
PRW_DATASF	0.0862511
MUON_ID	0.0790914
JET_CR_JET_JER_EffectiveNP_4	0.0693206
JET_CR_JET_Flavor_Response	0.0615697
JET_CR_JET_EffectiveNP_Mixed1	0.0614936
JET_CR_JET_JER_EffectiveNP_6	0.0533144
MUON_MS	0.0424074
MET_SoftTrk_ResoPara	0.0233498
JET_CR_JET_Flavor_Composition	0.0176095
MUON_SAGITTA_RESBIAS	0.00686623
JET_CR_JET_EtaIntercalibration_Modelling	0.00666156
JET_CR_JET_BJES_Response	0.00660339
JET_CR_JET_EffectiveNP_Modelling2	0.00659895
MUON_EFF_RECO_SYS	0.00502226
MET_SoftTrk_ResoPerp	0.00500272
JET_CR_JET_Pileup_RhoTopology	0.0048404
JET_CR_JET_EffectiveNP_Statistical1	0.00313513
JET_CR_JET_Pileup_OffsetMu	0.00298816
FT_EFF_Eigen_C_1_AntiKtVR30Rmax4Rmin02TrackJets_BTagging201903	0.00263794
JET_CR_JET_Pileup_OffsetNPV	0.00235843
JET_CR_JET_EffectiveNP_Modelling1	0.00167615
JET_CR_JET_EffectiveNP_Statistical3	0.00148708
JET_CR_JET_EffectiveNP_Mixed2	0.0013847
JET_CR_JET_EffectiveNP_Mixed3	0.00134235
JET_CR_JET_EffectiveNP_Modelling3	0.00129618
JET_CR_JET_Pileup_PtTerm	0.000965642
JET_CR_JET_EffectiveNP_Modelling4	0.000895054
FT_EFF_extrapolation_AntiKtVR30Rmax4Rmin02TrackJets_BTagging201903	0.00084331
JET_CR_JET_EtaIntercalibration_TotalStat	0.000569579
JET_CR_JET_EffectiveNP_Detector1	0.000494869
MUON_SCALE	0.000427381
JET_CR_JET_EffectiveNP_Statistical2	0.000292227
JET_CR_JET_EffectiveNP_Statistical4	0.000259656
FT_EFF_Eigen_Light_0_AntiKtVR30Rmax4Rmin02TrackJets_BTagging201903	0.000256668
FT_EFF_Eigen_C_0_AntiKtVR30Rmax4Rmin02TrackJets_BTagging201903	0.00025183
FT_EFF_Eigen_C_2_AntiKtVR30Rmax4Rmin02TrackJets_BTagging201903	0.000145096
FT_EFF_Eigen_Light_1_AntiKtVR30Rmax4Rmin02TrackJets_BTagging201903	0.000137404
FT_EFF_Eigen_B_1_AntiKtVR30Rmax4Rmin02TrackJets_BTagging201903	0.000122628
MUON_EFF_TTVA_SYS	0.000116294
FT_EFF_Eigen_B_0_AntiKtVR30Rmax4Rmin02TrackJets_BTagging201903	8.85223e-05
FT_EFF_extrapolation_from_charm_AntiKtVR30Rmax4Rmin02TrackJets_BTagging201903	8.63365e-05
JET_CR_JET_EffectiveNP_Statistical6	7.87187e-05
JET_CR_JET_EtaIntercalibration_NonClosure_negEta	7.39852e-05
MUON_EFF_TTVA_STAT	5.94475e-05
MUON_EFF_RECO_STAT	5.08114e-05
JET_CR_JET_EffectiveNP_Detector2	5.07814e-05
JET_CR_JET_EffectiveNP_Statistical5	3.98678e-05
FT_EFF_Eigen_B_2_AntiKtVR30Rmax4Rmin02TrackJets_BTagging201903	2.52605e-05
FT_EFF_Eigen_C_3_AntiKtVR30Rmax4Rmin02TrackJets_BTagging201903	5.44189e-06
MUON_EFF_RECO_SYS_LOWPT	4.65226e-06
FT_EFF_Eigen_Light_2_AntiKtVR30Rmax4Rmin02TrackJets_BTagging201903	7.39583e-07
MUON_EFF_RECO_STAT_LOWPT	5.66686e-07
FT_EFF_Eigen_Light_3_AntiKtVR30Rmax4Rmin02TrackJets_BTagging201903	1.63434e-07
FT_EFF_Eigen_Light_4_AntiKtVR30Rmax4Rmin02TrackJets_BTagging201903	1.36249e-08
EG_RESOLUTION_ALL	0.0
EG_SCALE_ALL	0.0
EL_EFF_ID_TOTAL_1NPCOR_PLUS_UNCOR	0.0
EL_EFF_Iso_TOTAL_1NPCOR_PLUS_UNCOR	0.0
EL_EFF_Reco_TOTAL_1NPCOR_PLUS_UNCOR	0.0
EL_EFF_Trigger_TOTAL_1NPCOR_PLUS_UNCOR	0.0
JET_CR_JET_EtaIntercalibration_NonClosure_highE	0.0
JET_CR_JET_EtaIntercalibration_NonClosure_posEta	0.0

continued on next page

Table A.2 – continued from previous page

Systematic	χ^2 1up
JET_CR_JET_PunchThrough_MC16	0.0
JET_CR_JET_SingleParticle_HighPt	0.0
JET_GR_JET_EffectiveNP_1	0.0
JET_GR_JET_EffectiveNP_2	0.0
JET_GR_JET_EffectiveNP_3	0.0
JET_GR_JET_EffectiveNP_4	0.0
JET_GR_JET_EffectiveNP_5	0.0
JET_GR_JET_EffectiveNP_6	0.0
JET_GR_JET_EffectiveNP_7restTerm	0.0
JET_GR_JET_Rscan_Dijet_DeltaR	0.0
JET_GR_JET_Rscan_Dijet_Isolation	0.0
JET_GR_JET_Rscan_Dijet_Jvt	0.0
JET_GR_JET_Rscan_Dijet_MC	0.0
JET_GR_JET_Rscan_Dijet_Stat	0.0
JET_GR_JET_Rscan_Zjet_DeltaR	0.0
JET_GR_JET_Rscan_Zjet_Isolation	0.0
JET_GR_JET_Rscan_Zjet_MC	0.0
JET_GR_JET_Rscan_Zjet_stat	0.0
JET_GR_JET_Zjet_Jvt	0.0
JET_JvtEfficiency	0.0
MUON_EFF_ISO_STAT	0.0
MUON_EFF_ISO_SYS	0.0
MUON_SAGITTA_RHO	0.0

Table A.3.: Ranking of the systematic uncertainties for the 1down variation of the $m^{HH}_{\text{vis+met}}$ discriminating distribution for the 2 TeV signal sample.

Systematic	χ^2 1down
JET_CR_JET_JER_EffectiveNP_2	0.250758
JET_CR_JET_JER_EffectiveNP_3	0.168757
JET_CR_JET_JER_EffectiveNP_1	0.1264
JET_CR_JET_JER_EffectiveNP_7restTerm	0.116226
JET_CR_JET_EffectiveNP_Mixed1	0.0946495
JET_CR_JET_JER_EffectiveNP_5	0.0885367
JET_CR_JET_JER_EffectiveNP_4	0.0693206
JET_CR_JET_Flavor_Response	0.0583545
JET_CR_JET_JER_EffectiveNP_6	0.0533144
PRW_DATASF	0.0315153
MUON_ID	0.0268517
MUON_SAGITTA_RESBIAS	0.0187033
MUON_MS	0.0156675
JET_CR_JET_Flavor_Composition	0.0125708
JET_CR_JET_EffectiveNP_Modelling2	0.0101183
JET_CR_JET_EtaIntercalibration_Modelling	0.00683711
JET_CR_JET_BJES_Response	0.00560926
MUON_EFF_RECO_SYS	0.00497527
JET_CR_JET_Pileup_OffsetMu	0.00478187
JET_CR_JET_EffectiveNP_Statistical1	0.00478134
JET_CR_JET_Pileup_RhoTopology	0.00460629
JET_CR_JET_Pileup_PtTerm	0.00316359
FT_EFF_Eigen_C_1_AntiKtVR30Rmax4Rmin02TrackJets_BTagging201903	0.0026349
JET_CR_JET_Pileup_OffsetNPV	0.00156975
JET_CR_JET_EffectiveNP_Statistical3	0.00148299
JET_CR_JET_EffectiveNP_Modelling1	0.00143542
JET_CR_JET_EffectiveNP_Mixed2	0.00137008
JET_CR_JET_EffectiveNP_Statistical4	0.0013231
JET_CR_JET_EffectiveNP_Statistical5	0.000979685
JET_CR_JET_EffectiveNP_Modelling3	0.000865553
JET_CR_JET_EtaIntercalibration_TotalStat	0.000752193
FT_EFF_extrapolation_AntiKtVR30Rmax4Rmin02TrackJets_BTagging201903	0.000678071
JET_CR_JET_EffectiveNP_Statistical6	0.000587181
MUON_SCALE	0.00041995

continued on next page

Table A.3 – continued from previous page

Systematic	χ^2 1down
FT_EFF_Eigen_Light_0_AntiKtVR30Rmax4Rmin02TrackJets_BTagging201903	0.000256019
FT_EFF_Eigen_C_0_AntiKtVR30Rmax4Rmin02TrackJets_BTagging201903	0.000251616
JET_CR_JET_EffectiveNP_Modelling4	0.000240565
JET_CR_JET_EffectiveNP_Mixed3	0.000237093
JET_CR_JET_EtaIntercalibration_NonClosure_posEta	0.000195976
JET_CR_JET_EffectiveNP_Detector1	0.000165716
JET_CR_JET_EffectiveNP_Detector2	0.000148069
FT_EFF_Eigen_C_2_AntiKtVR30Rmax4Rmin02TrackJets_BTagging201903	0.000145124
FT_EFF_Eigen_Light_1_AntiKtVR30Rmax4Rmin02TrackJets_BTagging201903	0.000137158
FT_EFF_Eigen_B_1_AntiKtVR30Rmax4Rmin02TrackJets_BTagging201903	0.000114658
MUON_EFF_TTVA_SYS	9.63824e-05
JET_CR_JET_EffectiveNP_Statistical2	9.07791e-05
FT_EFF_extrapolation_from_charm_AntiKtVR30Rmax4Rmin02TrackJets_BTagging201903	8.63202e-05
FT_EFF_Eigen_B_0_AntiKtVR30Rmax4Rmin02TrackJets_BTagging201903	8.39417e-05
EG_SCALE_ALL	7.3331e-05
MUON_EFF_TTVA_STAT	5.98298e-05
JET_CR_JET_EtaIntercalibration_NonClosure_negEta	5.84167e-05
MUON_EFF_RECO_STAT	5.07266e-05
FT_EFF_Eigen_B_2_AntiKtVR30Rmax4Rmin02TrackJets_BTagging201903	2.54998e-05
FT_EFF_Eigen_C_3_AntiKtVR30Rmax4Rmin02TrackJets_BTagging201903	5.43665e-06
MUON_EFF_RECO_SYS_LOWPT	4.65234e-06
MUON_EFF_RECO_STAT_LOWPT	8.55851e-07
FT_EFF_Eigen_Light_2_AntiKtVR30Rmax4Rmin02TrackJets_BTagging201903	7.24798e-07
FT_EFF_Eigen_Light_3_AntiKtVR30Rmax4Rmin02TrackJets_BTagging201903	1.60997e-07
FT_EFF_Eigen_Light_4_AntiKtVR30Rmax4Rmin02TrackJets_BTagging201903	1.27673e-08
EG_RESOLUTION_ALL	0.0
EL_EFF_ID_TOTAL_1NPCOR_PLUS_UNCOR	0.0
EL_EFF_Iso_TOTAL_1NPCOR_PLUS_UNCOR	0.0
EL_EFF_Reco_TOTAL_1NPCOR_PLUS_UNCOR	0.0
EL_EFF_Trigger_TOTAL_1NPCOR_PLUS_UNCOR	0.0
JET_CR_JET_EtaIntercalibration_NonClosure_highE	0.0
JET_CR_JET_PunchThrough_MC16	0.0
JET_CR_JET_SingleParticle_HighPt	0.0
JET_GR_JET_EffectiveNP_1	0.0
JET_GR_JET_EffectiveNP_2	0.0
JET_GR_JET_EffectiveNP_3	0.0
JET_GR_JET_EffectiveNP_4	0.0
JET_GR_JET_EffectiveNP_5	0.0
JET_GR_JET_EffectiveNP_6	0.0
JET_GR_JET_EffectiveNP_7restTerm	0.0
JET_GR_JET_Rscan_Dijet_DeltaR	0.0
JET_GR_JET_Rscan_Dijet_Isolation	0.0
JET_GR_JET_Rscan_Dijet_Jvt	0.0
JET_GR_JET_Rscan_Dijet_MC	0.0
JET_GR_JET_Rscan_Dijet_Stat	0.0
JET_GR_JET_Rscan_Zjet_DeltaR	0.0
JET_GR_JET_Rscan_Zjet_Isolation	0.0
JET_GR_JET_Rscan_Zjet_MC	0.0
JET_GR_JET_Rscan_Zjet_stat	0.0
JET_GR_JET_Zjet_Jvt	0.0
JET_JvtEfficiency	0.0
MUON_EFF_ISO_STAT	0.0
MUON_EFF_ISO_SYS	0.0
MUON_SAGITTA_RHO	0.0

Table A.4.: Ranking of the systematic uncertainties for the 1up variation of the $m^{HH}_{\text{vis+met}}$ discriminating distribution for the W+jets background sample.

Systematic	Reduced χ^2 1up
PRW_DATASF	0.325347
JET_CR_JET_JER_EffectiveNP_3	0.0503516
JET_CR_JET_JER_EffectiveNP_4	0.0497565
JET_CR_JET_JER_EffectiveNP_2	0.0452864
JET_CR_JET_JER_EffectiveNP_7restTerm	0.0443605

continued on next page

Table A.4 – continued from previous page

Systematic	Reduced χ^2 1up
JET_CR_JET_JER_EffectiveNP_5	0.0434099
JET_CR_JET_JER_EffectiveNP_1	0.0414553
JET_CR_JET_JER_EffectiveNP_6	0.0313023
MET_SoftTrk_ResoPara	0.0238225
JET_CR_JET_Flavor_Response	0.0200448
JET_CR_JET_EffectiveNP_Mixed1	0.0176127
MUON_ID	0.0117328
JET_CR_JET_BJES_Response	0.0100148
MUON_SAGITTA_RESBIAS	0.0100115
MUON_MS	0.00640406
JET_CR_JET_Pileup_PtTerm	0.00619075
JET_CR_JET_Pileup_OffsetNPV	0.00613408
JET_CR_JET_Pileup_RhoTopology	0.00609337
JET_CR_JET_Pileup_OffsetMu	0.00528134
JET_CR_JET_EtaIntercalibration_Modelling	0.00516486
JET_CR_JET_EffectiveNP_Modelling1	0.00500873
MET_SoftTrk_ResoPerp	0.00476139
JET_CR_JET_EffectiveNP_Modelling2	0.00456776
JET_CR_JET_EffectiveNP_Statistical1	0.00456776
JET_CR_JET_Flavor_Composition	0.00382833
JET_CR_JET_PunchThrough_MC16	0.00135464
JET_CR_JET_EffectiveNP_Mixed3	0.00113512
FT_EFF_extrapolation_AntiKtVR30Rmax4Rmin02TrackJets_BTagging201903	0.000633586
MUON_EFF_RECO_SYS	0.00018838
JET_CR_JET_EffectiveNP_Modelling3	0.00016235
JET_CR_JET_EtaIntercalibration_TotalStat	0.00016235
FT_EFF_Eigen_B_0_AntiKtVR30Rmax4Rmin02TrackJets_BTagging201903	0.000160356
MUON_EFF_RECO_SYS_LOWPT	8.00944e-05
FT_EFF_Eigen_C_1_AntiKtVR30Rmax4Rmin02TrackJets_BTagging201903	6.85446e-05
FT_EFF_Eigen_B_1_AntiKtVR30Rmax4Rmin02TrackJets_BTagging201903	5.22808e-05
FT_EFF_Eigen_Light_0_AntiKtVR30Rmax4Rmin02TrackJets_BTagging201903	3.92313e-05
FT_EFF_Eigen_Light_1_AntiKtVR30Rmax4Rmin02TrackJets_BTagging201903	3.17023e-05
FT_EFF_Eigen_C_0_AntiKtVR30Rmax4Rmin02TrackJets_BTagging201903	2.09248e-05
FT_EFF_Eigen_B_2_AntiKtVR30Rmax4Rmin02TrackJets_BTagging201903	1.44218e-05
FT_EFF_extrapolation_from_charm_AntiKtVR30Rmax4Rmin02TrackJets_BTagging201903	1.28243e-05
FT_EFF_Eigen_Light_2_AntiKtVR30Rmax4Rmin02TrackJets_BTagging201903	8.17543e-06
FT_EFF_Eigen_C_2_AntiKtVR30Rmax4Rmin02TrackJets_BTagging201903	6.15218e-06
MUON_EFF_TTVA_SYS	4.17332e-06
MUON_EFF_TTVA_STAT	2.56082e-06
MUON_EFF_RECO_STAT_LOWPT	2.34979e-06
MUON_EFF_RECO_STAT	2.31904e-06
FT_EFF_Eigen_C_3_AntiKtVR30Rmax4Rmin02TrackJets_BTagging201903	3.43481e-07
FT_EFF_Eigen_Light_3_AntiKtVR30Rmax4Rmin02TrackJets_BTagging201903	3.2028e-07
JET_CR_JET_EffectiveNP_Mixed2	1.48913e-07
JET_CR_JET_EffectiveNP_Statistical4	1.34085e-07
JET_CR_JET_EtaIntercalibration_NonClosure_posEta	1.34085e-07
FT_EFF_Eigen_Light_4_AntiKtVR30Rmax4Rmin02TrackJets_BTagging201903	1.82423e-08
EG_RESOLUTION_ALL	0.0
EG_SCALE_ALL	0.0
EL_EFF_ID_TOTAL_1NPCOR_PLUS_UNCOR	0.0
EL_EFF_Iso_TOTAL_1NPCOR_PLUS_UNCOR	0.0
EL_EFF_Reco_TOTAL_1NPCOR_PLUS_UNCOR	0.0
EL_EFF_Trigger_TOTAL_1NPCOR_PLUS_UNCOR	0.0
JET_CR_JET_EffectiveNP_Detector1	0.0
JET_CR_JET_EffectiveNP_Detector2	0.0
JET_CR_JET_EffectiveNP_Modelling4	0.0
JET_CR_JET_EffectiveNP_Statistical2	0.0
JET_CR_JET_EffectiveNP_Statistical3	0.0
JET_CR_JET_EffectiveNP_Statistical5	0.0
JET_CR_JET_EffectiveNP_Statistical6	0.0
JET_CR_JET_EtaIntercalibration_NonClosure_highE	0.0
JET_CR_JET_EtaIntercalibration_NonClosure_negEta	0.0
JET_CR_JET_SingleParticle_HighPt	0.0
JET_JvtEfficiency	0.0
MUON_EFF_ISO_STAT	0.0
MUON_EFF_ISO_SYS	0.0
MUON_SAGITTA_RHO	0.0
MUON_SCALE	0.0

Table A.5.: Ranking of the systematic uncertainties for the 1down variation of the $m^{HH}_{\text{vis+met}}$ discriminating distribution for the W+jets background sample.

Systematic	Reduced χ^2 1down
PRW_DATASF	0.134785
JET_CR_JET_JER_EffectiveNP_3	0.0503516
JET_CR_JET_JER_EffectiveNP_4	0.0497565
JET_CR_JET_JER_EffectiveNP_2	0.0452864
JET_CR_JET_JER_EffectiveNP_7restTerm	0.0443605
JET_CR_JET_JER_EffectiveNP_5	0.0434099
JET_CR_JET_JER_EffectiveNP_1	0.0414553
JET_CR_JET_JER_EffectiveNP_6	0.0313023
JET_CR_JET_Flavor_Response	0.0151455
JET_CR_JET_Flavor_Composition	0.00906095
JET_CR_JET_EtaIntercalibration_Modelling	0.00830552
JET_CR_JET_Pileup_RhoTopology	0.00651742
JET_CR_JET_Pileup_OffsetNPV	0.00451453
MUON_ID	0.00367177
MUON_SAGITTA_RESBIAS	0.00360257
JET_CR_JET_Pileup_OffsetMu	0.00324152
JET_CR_JET_EffectiveNP_Mixed1	0.00314042
MUON_MS	0.00262543
JET_CR_JET_BJES_Response	0.00170333
FT_EFF_extrapolation_AntiKtVR30Rmax4Rmin02TrackJets_BTagging201903	0.000632955
JET_CR_JET_EffectiveNP_Modelling2	0.000539939
JET_CR_JET_EffectiveNP_Statistical1	0.000539939
JET_CR_JET_EffectiveNP_Modelling1	0.000316758
JET_CR_JET_EffectiveNP_Mixed3	0.000277545
JET_CR_JET_Pileup_PtTerm	0.000277545
MUON_SCALE	0.000262394
MUON_EFF_RECO_SYS	0.000186997
FT_EFF_Eigen_B_0_AntiKtVR30Rmax4Rmin02TrackJets_BTagging201903	0.000169464
JET_CR_JET_EffectiveNP_Statistical4	0.00016235
JET_CR_JET_EffectiveNP_Statistical5	0.00016235
MUON_EFF_RECO_SYS_LOWPT	8.0094e-05
FT_EFF_Eigen_C_1_AntiKtVR30Rmax4Rmin02TrackJets_BTagging201903	7.60751e-05
FT_EFF_Eigen_B_1_AntiKtVR30Rmax4Rmin02TrackJets_BTagging201903	5.32805e-05
JET_CR_JET_EffectiveNP_Mixed2	5.03986e-05
FT_EFF_Eigen_Light_0_AntiKtVR30Rmax4Rmin02TrackJets_BTagging201903	3.89369e-05
FT_EFF_Eigen_Light_1_AntiKtVR30Rmax4Rmin02TrackJets_BTagging201903	3.17039e-05
FT_EFF_Eigen_C_0_AntiKtVR30Rmax4Rmin02TrackJets_BTagging201903	2.08618e-05
JET_CR_JET_PunchThrough_MC16	1.49093e-05
FT_EFF_Eigen_B_2_AntiKtVR30Rmax4Rmin02TrackJets_BTagging201903	1.42556e-05
FT_EFF_extrapolation_from_charm_AntiKtVR30Rmax4Rmin02TrackJets_BTagging201903	1.28246e-05
FT_EFF_Eigen_Light_2_AntiKtVR30Rmax4Rmin02TrackJets_BTagging201903	8.19684e-06
FT_EFF_Eigen_C_2_AntiKtVR30Rmax4Rmin02TrackJets_BTagging201903	6.3531e-06
MUON_EFF_TTVA_SYS	3.40232e-06
MUON_EFF_TTVA_STAT	2.56044e-06
MUON_EFF_RECO_STAT_LOWPT	2.43732e-06
MUON_EFF_RECO_STAT	2.31905e-06
FT_EFF_Eigen_C_3_AntiKtVR30Rmax4Rmin02TrackJets_BTagging201903	3.41226e-07
FT_EFF_Eigen_Light_3_AntiKtVR30Rmax4Rmin02TrackJets_BTagging201903	3.20592e-07
FT_EFF_Eigen_Light_4_AntiKtVR30Rmax4Rmin02TrackJets_BTagging201903	1.82968e-08
EG_RESOLUTION_ALL	0.0
EG_SCALE_ALL	0.0
EL_EFF_ID_TOTAL_1NPCOR_PLUS_UNCOR	0.0
EL_EFF_Iso_TOTAL_1NPCOR_PLUS_UNCOR	0.0
EL_EFF_Reco_TOTAL_1NPCOR_PLUS_UNCOR	0.0
EL_EFF_Trigger_TOTAL_1NPCOR_PLUS_UNCOR	0.0
JET_CR_JET_EffectiveNP_Detector1	0.0
JET_CR_JET_EffectiveNP_Detector2	0.0
JET_CR_JET_EffectiveNP_Modelling3	0.0
JET_CR_JET_EffectiveNP_Modelling4	0.0
JET_CR_JET_EffectiveNP_Statistical2	0.0
JET_CR_JET_EffectiveNP_Statistical3	0.0
JET_CR_JET_EffectiveNP_Statistical6	0.0
JET_CR_JET_EtaIntercalibration_NonClosure_highE	0.0
JET_CR_JET_EtaIntercalibration_NonClosure_negEta	0.0
JET_CR_JET_EtaIntercalibration_NonClosure_posEta	0.0
JET_CR_JET_EtaIntercalibration_TotalStat	0.0
JET_CR_JET_SingleParticle_HighPt	0.0

continued on next page

Table A.5 – continued from previous page

Systematic	Reduced χ^2 1down
JET_JvtEfficiency	0.0
MUON_EFF_ISO_STAT	0.0
MUON_EFF_ISO_SYS	0.0
MUON_SAGITTA_RHO	0.0

A.3. Results $t\bar{t}$ background process

A.3.1. Kinematic distributions

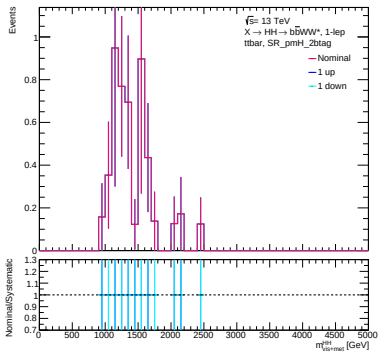

(a) $m^{HH}_{\mathrm{vis+met}}$

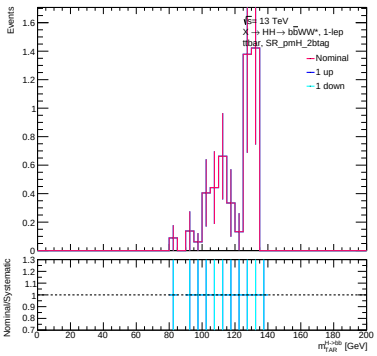

(b) $m^{H\to b\bar{b}}_{\mathrm{TAR}}$

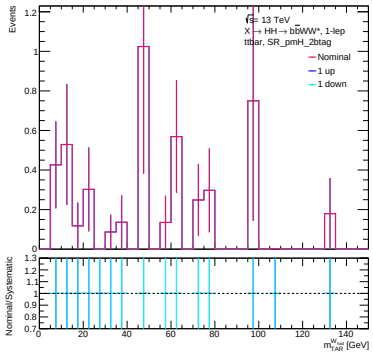

(c) $m^{W_{\mathrm{had}}}_{\mathrm{TAR}}$

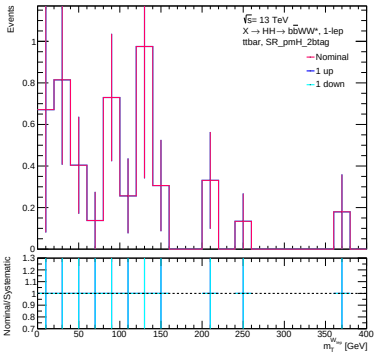

(d) $m^{W_{\mathrm{lep}}}_{T}$

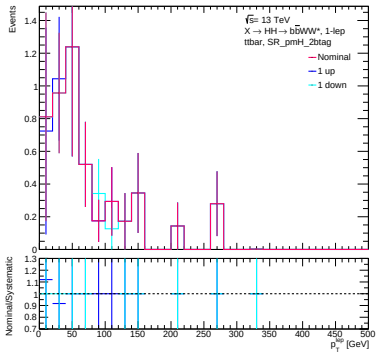

(e) p^{ℓ}_{T}

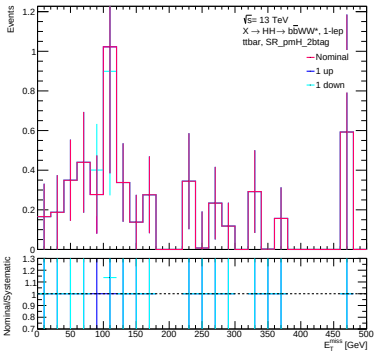

(f) E^{miss}_{T}

Figure A.1.: Kinematic distributions for the muon momentum resolution systematic uncertainty for the $t\bar{t}$ background sample.

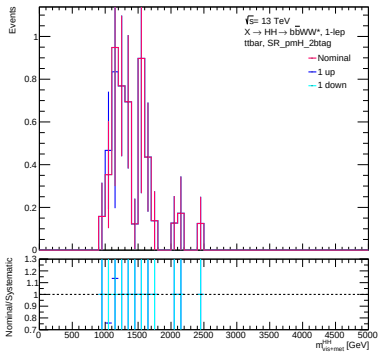

(a) $m_{\mathrm{vis+met}}^{HH}$

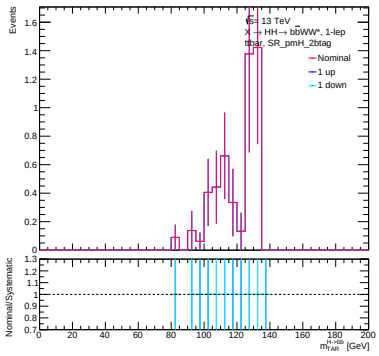

(b) $m_{\mathrm{TAR}}^{H\to b\bar{b}}$

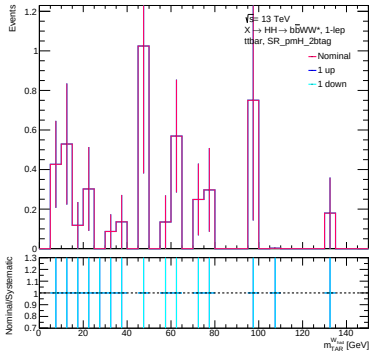

(c) $m_{\mathrm{TAR}}^{W_{\mathrm{had}}}$

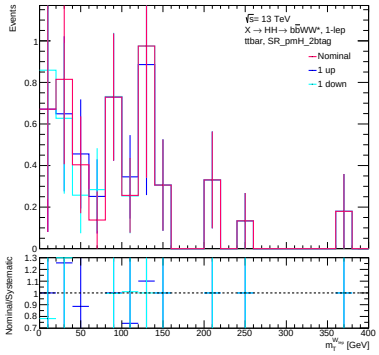

(d) $m_{T}^{W_{\mathrm{lep}}}$

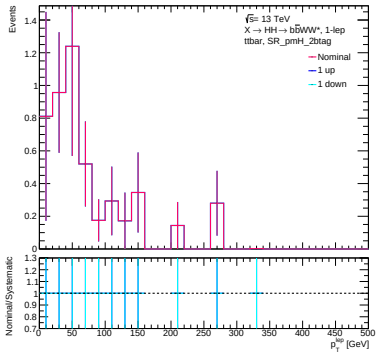

(e) p_{T}^{ℓ}

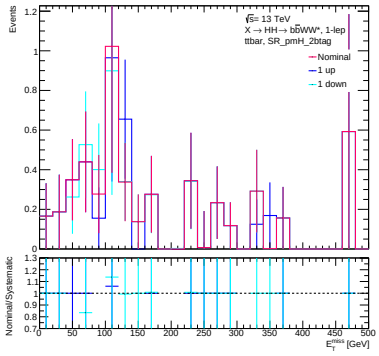

(f) E_{T}^{miss}

Figure A.2.: Kinematic distributions for the jet energy scale flavour composition systematic uncertainty for the $t\bar{t}$ background sample.

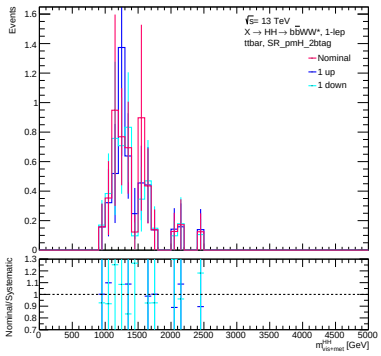

(a) $m_{\mathrm{vis+met}}^{HH}$

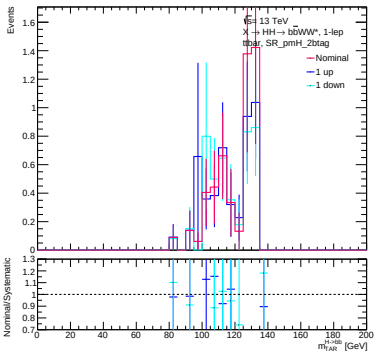

(b) $m_{\mathrm{TAR}}^{H\to b\bar{b}}$

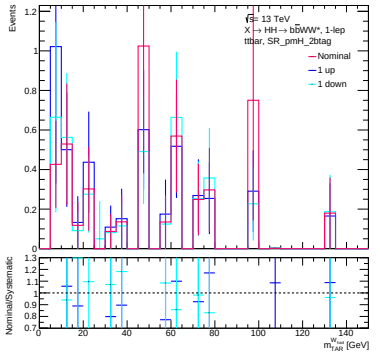

(c) $m_{\mathrm{TAR}}^{W_{\mathrm{had}}}$

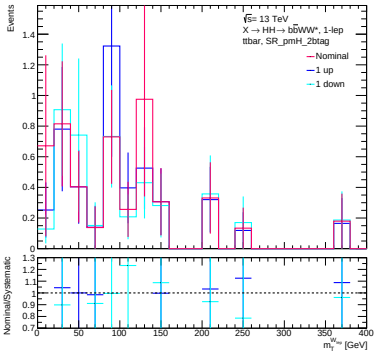

(d) $m_{T}^{W_{\mathrm{lep}}}$

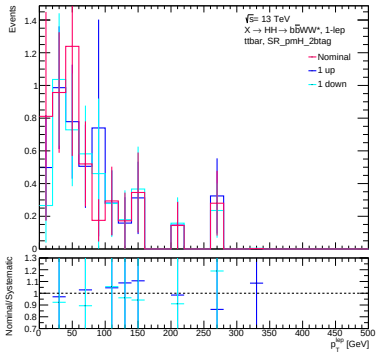

(e) p_T^{ℓ}

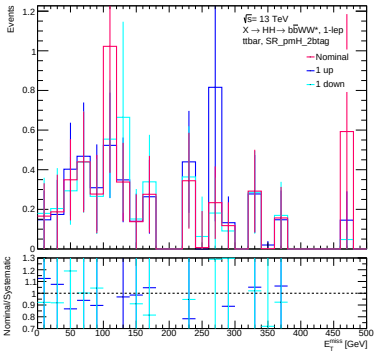

(f) E_T^{miss}

Figure A.3.: Kinematic distributions for the pileup reweighting uncertainty for the $t\bar{t}$ background sample.

A.3.2. Systematic uncertainties rankings

Table A.6.: Ranking of the systematic uncertainties for the 1up variation of the $m_{\text{vis+met}}^{HH}$ discriminating distribution for the $t\bar{t}$ background sample.

Systematic	Reduced χ^2 1up
PRW_DATASF	0.110163
JET_CR_JET_JER_EffectiveNP_1	0.0353488
JET_CR_JET_JER_EffectiveNP_2	0.0353488
JET_CR_JET_JER_EffectiveNP_3	0.0309382
JET_CR_JET_JER_EffectiveNP_7restTerm	0.00529238
MET_SoftTrk_ResoPara	0.00482364
JET_CR_JET_EffectiveNP_Modelling1	0.00473824
JET_CR_JET_Flavor_Composition	0.00473824
JET_CR_JET_Pileup_OffsetNPV	0.00473824
MET_SoftTrk_ResoPerp	0.00473824
FT_EFF_extrapolation_AntiKtVR30Rmax4Rmin02TrackJets_BTagging201903	0.00430302
FT_EFF_Eigen_B_0_AntiKtVR30Rmax4Rmin02TrackJets_BTagging201903	0.000332338
FT_EFF_Eigen_B_1_AntiKtVR30Rmax4Rmin02TrackJets_BTagging201903	0.000316424
FT_EFF_Eigen_B_2_AntiKtVR30Rmax4Rmin02TrackJets_BTagging201903	0.000113254
FT_EFF_Eigen_C_1_AntiKtVR30Rmax4Rmin02TrackJets_BTagging201903	3.17137e-05
MUON_EFF_RECO_SYS	1.21246e-05
FT_EFF_extrapolation_from_charm_AntiKtVR30Rmax4Rmin02TrackJets_BTagging201903	7.52066e-06
JET_CR_JET_JER_EffectiveNP_4	4.14054e-06
JET_CR_JET_JER_EffectiveNP_5	4.14054e-06
JET_CR_JET_JER_EffectiveNP_6	4.14054e-06
FT_EFF_Eigen_C_0_AntiKtVR30Rmax4Rmin02TrackJets_BTagging201903	4.00078e-06
MUON_EFF_RECO_STAT	1.79889e-06
FT_EFF_Eigen_C_2_AntiKtVR30Rmax4Rmin02TrackJets_BTagging201903	1.17834e-06
MUON_EFF_RECO_SYS_LOWPT	1.08944e-06
MUON_EFF_RECO_STAT_LOWPT	9.37794e-07
MUON_EFF_TTVA_STAT	5.29861e-07
MUON_EFF_TTVA_SYS	3.55444e-07
FT_EFF_Eigen_Light_0_AntiKtVR30Rmax4Rmin02TrackJets_BTagging201903	2.40272e-07
FT_EFF_Eigen_Light_1_AntiKtVR30Rmax4Rmin02TrackJets_BTagging201903	4.57908e-08
FT_EFF_Eigen_C_3_AntiKtVR30Rmax4Rmin02TrackJets_BTagging201903	3.29103e-08
FT_EFF_Eigen_Light_2_AntiKtVR30Rmax4Rmin02TrackJets_BTagging201903	2.2664e-08
FT_EFF_Eigen_Light_3_AntiKtVR30Rmax4Rmin02TrackJets_BTagging201903	1.20858e-09
FT_EFF_Eigen_Light_4_AntiKtVR30Rmax4Rmin02TrackJets_BTagging201903	1.57356e-11
EG_RESOLUTION_ALL	0.0
EG_SCALE_ALL	0.0
EL_EFF_ID_TOTAL_1NPCOR_PLUS_UNCOR	0.0
EL_EFF_Iso_TOTAL_1NPCOR_PLUS_UNCOR	0.0
EL_EFF_Reco_TOTAL_1NPCOR_PLUS_UNCOR	0.0
EL_EFF_Trigger_TOTAL_1NPCOR_PLUS_UNCOR	0.0
JET_CR_JET_BJES_Response	0.0
JET_CR_JET_EffectiveNP_Detector1	0.0
JET_CR_JET_EffectiveNP_Detector2	0.0
JET_CR_JET_EffectiveNP_Mixed1	0.0
JET_CR_JET_EffectiveNP_Mixed2	0.0
JET_CR_JET_EffectiveNP_Mixed3	0.0
JET_CR_JET_EffectiveNP_Modelling2	0.0
JET_CR_JET_EffectiveNP_Modelling3	0.0
JET_CR_JET_EffectiveNP_Modelling4	0.0
JET_CR_JET_EffectiveNP_Statistical1	0.0
JET_CR_JET_EffectiveNP_Statistical2	0.0
JET_CR_JET_EffectiveNP_Statistical3	0.0
JET_CR_JET_EffectiveNP_Statistical4	0.0
JET_CR_JET_EffectiveNP_Statistical5	0.0
JET_CR_JET_EffectiveNP_Statistical6	0.0
JET_CR_JET_EtaIntercalibration_Modelling	0.0
JET_CR_JET_EtaIntercalibration_NonClosure_highE	0.0
JET_CR_JET_EtaIntercalibration_NonClosure_negEta	0.0
JET_CR_JET_EtaIntercalibration_NonClosure_posEta	0.0
JET_CR_JET_EtaIntercalibration_TotalStat	0.0
JET_CR_JET_Flavor_Response	0.0
JET_CR_JET_Pileup_OffsetMu	0.0
JET_CR_JET_Pileup_PtTerm	0.0
JET_CR_JET_Pileup_RhoTopology	0.0
JET_CR_JET_PunchThrough_MC16	0.0

continued on next page

Table A.6 – continued from previous page

Systematic	Reduced χ^2 1up
JET_CR_JET_SingleParticle_HighPt	0.0
JET_JvtEfficiency	0.0
MUON_EFF_ISO_STAT	0.0
MUON_EFF_ISO_SYS	0.0
MUON_ID	0.0
MUON_MS	0.0
MUON_SAGITTA_RESBIAS	0.0
MUON_SAGITTA_RHO	0.0
MUON_SCALE	0.0

Table A.7.: Ranking of the systematic uncertainties for the 1down variation of the $m^{HH}_{\text{vis+met}}$ discriminating distribution for the $t\bar{t}$ background sample.

Systematic	Reduced χ^2 1down
JET_CR_JET_JER_EffectiveNP_1	0.0353488
JET_CR_JET_JER_EffectiveNP_2	0.0353488
JET_CR_JET_JER_EffectiveNP_3	0.0309382
PRW_DATASF	0.0250569
JET_CR_JET_JER_EffectiveNP_7restTerm	0.00529238
JET_CR_JET_BJES_Response	0.00473824
JET_CR_JET_EffectiveNP_Mixed1	0.00473824
JET_CR_JET_EffectiveNP_Modelling2	0.00473824
JET_CR_JET_EffectiveNP_Statistical1	0.00473824
JET_CR_JET_Flavor_Response	0.00473824
FT_EFF_extrapolation_AntiKtVR30Rmax4Rmin02TrackJets_BTagging201903	0.00430302
FT_EFF_Eigen_B_0_AntiKtVR30Rmax4Rmin02TrackJets_BTagging201903	0.00033032
FT_EFF_Eigen_B_1_AntiKtVR30Rmax4Rmin02TrackJets_BTagging201903	0.000317642
FT_EFF_Eigen_B_2_AntiKtVR30Rmax4Rmin02TrackJets_BTagging201903	0.000113024
FT_EFF_Eigen_C_1_AntiKtVR30Rmax4Rmin02TrackJets_BTagging201903	3.17281e-05
MUON_EFF_RECO_SYS	1.20321e-05
FT_EFF_extrapolation_from_charm_AntiKtVR30Rmax4Rmin02TrackJets_BTagging201903	7.52064e-06
JET_CR_JET_JER_EffectiveNP_4	4.14054e-06
JET_CR_JET_JER_EffectiveNP_5	4.14054e-06
JET_CR_JET_JER_EffectiveNP_6	4.14054e-06
FT_EFF_Eigen_C_0_AntiKtVR30Rmax4Rmin02TrackJets_BTagging201903	4.01369e-06
MUON_EFF_RECO_STAT	1.79892e-06
FT_EFF_Eigen_C_2_AntiKtVR30Rmax4Rmin02TrackJets_BTagging201903	1.18136e-06
MUON_EFF_RECO_SYS_LOWPT	1.0895e-06
MUON_EFF_RECO_STAT_LOWPT	9.50607e-07
MUON_EFF_TTVA_STAT	5.29931e-07
MUON_EFF_TTVA_SYS	3.37237e-07
FT_EFF_Eigen_Light_0_AntiKtVR30Rmax4Rmin02TrackJets_BTagging201903	2.39947e-07
FT_EFF_Eigen_Light_1_AntiKtVR30Rmax4Rmin02TrackJets_BTagging201903	4.58797e-08
FT_EFF_Eigen_C_3_AntiKtVR30Rmax4Rmin02TrackJets_BTagging201903	3.29595e-08
FT_EFF_Eigen_Light_2_AntiKtVR30Rmax4Rmin02TrackJets_BTagging201903	2.2657e-08
FT_EFF_Eigen_Light_3_AntiKtVR30Rmax4Rmin02TrackJets_BTagging201903	1.20826e-09
FT_EFF_Eigen_Light_4_AntiKtVR30Rmax4Rmin02TrackJets_BTagging201903	1.57564e-11
EG_RESOLUTION_ALL	0.0
EG_SCALE_ALL	0.0
EL_EFF_ID_TOTAL_1NPCOR_PLUS_UNCOR	0.0
EL_EFF_Iso_TOTAL_1NPCOR_PLUS_UNCOR	0.0
EL_EFF_Reco_TOTAL_1NPCOR_PLUS_UNCOR	0.0
EL_EFF_Trigger_TOTAL_1NPCOR_PLUS_UNCOR	0.0
JET_CR_JET_EffectiveNP_Detector1	0.0
JET_CR_JET_EffectiveNP_Detector2	0.0
JET_CR_JET_EffectiveNP_Mixed2	0.0
JET_CR_JET_EffectiveNP_Mixed3	0.0
JET_CR_JET_EffectiveNP_Modelling1	0.0
JET_CR_JET_EffectiveNP_Modelling3	0.0
JET_CR_JET_EffectiveNP_Modelling4	0.0
JET_CR_JET_EffectiveNP_Statistical2	0.0
JET_CR_JET_EffectiveNP_Statistical3	0.0
JET_CR_JET_EffectiveNP_Statistical4	0.0
JET_CR_JET_EffectiveNP_Statistical5	0.0

continued on next page

Table A.7 – continued from previous page

Systematic	Reduced χ^2 1down
JET_CR_JET_EffectiveNP_Statistical6	0.0
JET_CR_JET_EtaIntercalibration_Modelling	0.0
JET_CR_JET_EtaIntercalibration_NonClosure_highE	0.0
JET_CR_JET_EtaIntercalibration_NonClosure_negEta	0.0
JET_CR_JET_EtaIntercalibration_NonClosure_posEta	0.0
JET_CR_JET_EtaIntercalibration_TotalStat	0.0
JET_CR_JET_Flavor_Composition	0.0
JET_CR_JET_Pileup_OffsetMu	0.0
JET_CR_JET_Pileup_OffsetNPV	0.0
JET_CR_JET_Pileup_PtTerm	0.0
JET_CR_JET_Pileup_RhoTopology	0.0
JET_CR_JET_PunchThrough_MC16	0.0
JET_CR_JET_SingleParticle_HighPt	0.0
JET_JvtEfficiency	0.0
MUON_EFF_ISO_STAT	0.0
MUON_EFF_ISO_SYS	0.0
MUON_ID	0.0
MUON_MS	0.0
MUON_SAGITTA_RESBIAS	0.0
MUON_SAGITTA_RHO	0.0
MUON_SCALE	0.0

Table A.8.: Systematic uncertainties with the largest impact for each of the considered kinematic distributions for the $t\bar{t}$ background sample.

Distribution	1up variation	1down variation
$m_{\text{vis+met}}^{HH}$	pileup reweighting uncertainty	jet energy resolution uncertainty (1)
E_T^{miss}	jet energy scale uncertainty (flavour composition)	jet energy resolution uncertainty (2)
$m_T^{W_{\text{lep}}}$	pileup reweighting uncertainty	jet energy resolution uncertainty (2)
$m_{\text{TAR}}^{H\to b\bar{b}}$	pileup reweighting uncertainty	pileup reweighting uncertainty
$m_{\text{TAR}}^{W_{\text{had}}}$	pileup reweighting uncertainty	pileup reweighting uncertainty
p_T^{ℓ}	pileup reweighting uncertainty	pileup reweighting uncertainty

Bibliography

[1] ATLAS Collaboration, *Observation of a new particle in the search for the Standard Model Higgs boson with the ATLAS detector at the LHC*, Physics Letters B **716(1)**, 1 (2012)

[2] CMS Collaboration, *Observation of a new boson at a mass of 125 GeV with the CMS experiment at the LHC*, Physics Letters B **716(1)**, 30 (2012)

[3] F. Englert, R. Brout, *Broken Symmetry and the Mass of Gauge Vector Mesons*, Phys. Rev. Lett. **13**, 321 (1964)

[4] P. W. Higgs, *Broken Symmetries and the Masses of Gauge Bosons*, Phys. Rev. Lett. **13**, 508 (1964)

[5] *Standard Model of Elementary Particles*, `https://en.wikipedia.org/wiki/File:Standard_Model_of_Elementary_Particles.svg`, Accessed: 2021-03-28

[6] M. K. Gaillard, P. D. Grannis, F. J. Sciulli, *The standard model of particle physics*, volume 71, pages 96–111, American Physical Society (APS) (1999)

[7] W. Hollik, *Quantum field theory and the Standard Model*, in *2009 European School of High-Energy Physics* (2010), `arXiv:hep-ph/1012.3883`

[8] M. Thomson, *Modern Particle Physics*, Cambridge University Press (2013)

[9] P. Zyla, et al. (Particle Data Group), *Review of Particle Physics*, PTEP **2020(8)**, 083C01 (2020)

[10] S. L. Glashow, *Partial Symmetries of Weak Interactions*, Nucl. Phys. **22**, 579 (1961)

[11] S. Weinberg, *A Model of Leptons*, Phys. Rev. Lett. **19**, 1264 (1967)

[12] A. Salam, J. Ward, *Electromagnetic and weak interactions*, Phys. Lett. **13(2)**, 168 (1964)

[13] ATLAS Collaboration, CMS Collaboration, *Combined Measurement of the Higgs Boson Mass in pp Collisions at $\sqrt{s} = 7$ TeV and $\sqrt{s} = 8$ TeV with the ATLAS and CMS Experiments*, Phys. Rev. Lett. **114(19)** (2015)

[14] D. de Florian, et al. (LHC Higgs Cross Section Working Group), *Handbook of LHC Higgs Cross Sections: 4. Deciphering the Nature of the Higgs Sector* **2/2017** (2016), 1610.07922

[15] A. Djouadi, *The anatomy of electroweak symmetry breaking Tome II: The Higgs bosons in the Minimal Supersymmetric Model*, Phys. Rep. **459(1-6)**, 1 (2008)

[16] E. W. Kolb, M. S. Turner, *The Early Universe*, CRC Press (1990)

[17] C. Csáki, *The Minimal Supersymmetric Standard Model (MSSM)*, Mod. Phys. Lett. A **11(08)**, 599 (1996)

[18] G. Branco, et al., *Theory and phenomenology of two-Higgs-doublet models*, Physics Reports **516(1-2)**, 1 (2012)

[19] L. Fromme, S. J. Huber, M. Seniuch, *Baryogenesis in the two-Higgs doublet model*, JHEP **2006(11)** (2006)

[20] ATLAS Collaboration, *Search for Higgs boson pair production in the $b\bar{b}WW^*$ decay mode at $\sqrt{s}$= 13 TeV with the ATLAS detector*, Journal of High Energy Physics **2019(4)** (2019)

[21] M. Grazzini, et al., *Higgs boson pair production at NNLO with top quark mass effects*, JHEP **2018(5)** (2018)

[22] ATLAS Collaboration, *Searches for Higgs boson pair production in the $hh \rightarrow bb\tau\tau, \gamma\gamma WW^*, \gamma\gamma bb, bbbb$ channels with the ATLAS detector*, Physical Review D **92(9)** (2015)

[23] E. Mobs, *The CERN accelerator complex - 2019. Complexe des accélérateurs du CERN - 2019* (2019), general Photo, URL http://cds.cern.ch/record/2684277

[24] L. Evans, P. Bryant, *LHC Machine*, JINST **3**, S08001 (2008)

[25] ATLAS Collaboration, *The ATLAS Experiment at the CERN Large Hadron Collider*, JINST **3**, S08003 (2008)

[26] ATLAS Collaboration, *Search for resonant boosted SH and HH production in the $b\bar{b}VV^*$ decay channel with 0 or 1 lepton in the final state using the full Run 2 ATLAS data* (2021), ATLAS Note ANA-HDBS-2019-03-INT1

[27] M. Cacciari, G. P. Salam, G. Soyez, *The anti-k_t jet clustering algorithm*, JHEP **2008(04)** (2008)

[28] ATLAS Collaboration, *Track assisted techniques for jet substructure*, ATL-PHYS-PUB-2018-012, CERN, Geneva (2018)

[29] M. Cacciari, G. P. Salam, G. Soyez, *The catchment area of jets*, JHEP **2008(04)**, 005 (2008)

[30] ATLAS Collaboration, *Optimisation and performance studies of the ATLAS b-tagging algorithms for the 2017-18 LHC run*, ATL-PHYS-PUB-2017-013, CERN, Geneva (2020)

[31] I. Béjar Alonso et al., *High-Luminosity Large Hadron Collider (HL-LHC): Technical design report*, CERN Yellow Reports: Monographs, CERN, Geneva (2020)

Acknowledgements

Writing my thesis at the II. Institute of Physics has allowed me to get an insight into experimental particle physics research and I would like to take the opportunity to thank the people who made this possible.

Stan, I could not have wished for better supervision or a research group to write my thesis in. **Thank you** for all the time you invested, starting with the internship, the weekly research chats, to providing feedback on the thesis towards the end. It has been a great experience and I have felt very welcome.

Jason, you always found the time for a chat, in your days which seem to be completely filled with meetings. I am very grateful for this, the chats helped immensely with getting started in the beginning and staying on track later on. **Thank you** for all the advise and feedback not only on the thesis itself but also on the many presentations.

Kira, you always took the time to answer all my questions regarding the framework and the analysis, whether it was at 7 am or 10 pm. **Thank you** for this and for producing new samples over and over again even though they filled up all of our disc space by the end. I wish you all the best with your upcoming PhD thesis.

Zum Schluss, ein dickes **Danke** an meine Familie und an das Team Kuchen für eure Unterstützung während des letzten Semesters.

Erklärung nach §13(9) der Prüfungsordnung für den Bachelor-Studiengang Physik und den Master-Studiengang Physik an der Universität Göttingen:
Hiermit erkläre ich, dass ich diese Abschlussarbeit selbständig verfasst habe, keine anderen als die angegebenen Quellen und Hilfsmittel benutzt habe und alle Stellen, die wörtlich oder sinngemäß aus veröffentlichten Schriften entnommen wurden, als solche kenntlich gemacht habe.
Darüberhinaus erkläre ich, dass diese Abschlussarbeit nicht, auch nicht auszugsweise, im Rahmen einer nichtbestandenen Prüfung an dieser oder einer anderen Hochschule eingereicht wurde.

Göttingen, den 14. September 2021

(Janne van den Hout)